TÉCNICO LISBOA

Design Estimation of Multirotor for Heliostat Cleaning Purposes

Valentina Herrera Tchernykh

Thesis to obtain the Master of Science Degree in

Energy Engineering and Management

Supervisors: Dr. Alberto Manuel Martinho Vale
Dr. Willie Smit

Examination Committee

Chairperson: Prof. Luís Filipe Moreira Mendes
Supervisor: Dr. Alberto Manuel Martinho Vale
Member of the Committee: Prof. Bruno João Nogueira Guerreiro

January 2020

Acknowledgments

I am grateful to my mother and father, who have provided me with moral, emotional and educational support in my life and who have encourage me to pursue my passions. I am also grateful to my other family members and friends who have supported me along the way.

Thank you to my supervisors, Alberto Vale and Willie Smit, as well as the president of the jury, Luis Filipe Mendes, for providing guidance and feedback throughout this project. A very special gratitude to all those down at STERG for helping and providing the possibility of the work.

And finally, last but by no means least, thank you Marco for your unfailing support. Without you I would not have been able to complete this research, and I would not have made it through my masters degree!

Thanks for all your support and encouragement!

Abstract

It is becoming ever more important the automation of concentrated solar power (CSP) plants' monitoring and cleaning procedures, especially for plants remotely located where it is hard for manpower to reach and maintain in addition to the growth in cost of human resources. At the same time, it is necessary to improve the traditional heliostat cleaning methods in order to use the least water possible avoiding methods that may damage the heliostats. The objective of the presented work is to estimate the optimal way of utilizing ultrasonic cleaning devices with multirotors for heliostat cleaning purposes.

The developed model is a suitable high-level estimation for choosing a multirotor whose purpose is to transport one or several cleaning devices through a CSP heliostat field. The model was developed to simulate the payload capability in relation to the power required for a multirotor to make the optimal path for transporting one or several cleaning devices through all the heliostat field. The work is divided in two submodels.

The first submodel considers a specific example field to model and identify the optimal path and behavior of the multirotor to distribute a determined amount of cleaning device(s). The design of the path will include placement of battery charging and water refiling station (fixed or transportable), docking and flying sketch.

The second submodel focuses on simulating different parameters of the multirotor such as motor, rotor diameter, battery size and total multirotor weight, to find the optimal trade-off between the flying time and payload weight.

Keywords: *UAV, Multirotor, Flight-time, Payload, Heliostat, Cleaning.*

Resumo

É emergente a automatização dos procedimentos de inspeção e limpeza das centrais de Energia Solar de Concentração (CSP), principalmente em centrais localizadas remotamente e de difícil acesso, para além dos elevados recursos humanos. Ao mesmo tempo, é necessário melhorar os métodos tradicionais de limpeza de helióstatos, de forma a minimizar a quantidade de água necessária para limpeza e mitigar os riscos de deterioração propositada.

O objetivo do trabalho apresentado é estimar a melhor maneira de utilizar dispositivos de limpeza ultrassónicos transportados por multirotores para fins de limpeza de helióstatos. Um modelo para um multirotor ideal foi desenvolvido para simular a capacidade de carga útil em relação à potência necessária para percorrer o caminho ótimo para o transporte de um ou vários dispositivos de limpeza por todo o campo de helióstatos.

O trabalho está dividido em dois modelos principais. O primeiro modelo consiste em identificar o caminho ótimo para distribuir uma determinada quantidade de dispositivos de limpeza ao longo de uma central de CSP. O caminho inclui a deslocação à estação de carregamento de bateria e de abastecimento de água, bem como os procedimentos de descolagem, voo e aterragem. O segundo modelo simula os diferentes parâmetros do multirotor, nomeadamente potência do motor, diâmetro do rotor, características da bateria e peso total, para encontrar o melhor equilíbrio entre o tempo de voo e a capacidade de carga para transporte.

Palavras-chave: *UAV, Multirotor, Flight-time, Payload, Heliostat, Cleaning.*

Contents

Acknowledgments iii

Abstract iv

Resumo v

List of Figures ix

List of Tables x

Nomenclature xii

Glossary xii

1 Introduction 1

1.1 Background . . . 1

1.1.1 CSP Technology . . . 1

1.1.2 Heliostat Cleaning . . . 2

1.1.3 UVAs for Operational and Maintenance of Solar Energy Plants . . . 3

1.2 Motivation . . . 3

1.3 Objectives . . . 4

1.4 Methodology . . . 4

1.5 Outline . . . 5

2 Literature Review 7

2.1 State of Art: Heliostat Cleaning Technologies . . . 7

2.1.1 Traditional Methods . . . 7

2.1.2 New Methods . . . 8

2.2 State of Art: UAVs Design Methods . . . 9

2.3 Theoretical Overview of Multirotor Functionalities . . . 11

2.4 Aerodynamics . . . 12

2.4.1 Momentum Theory . . . 12

2.4.2 Blade Element Theory . . . 14

2.4.3 Figure of Merit 17

3 Modeling **20**

3.1 Flight-Path Model 22

3.1.1 Outputs and Inputs 23

3.1.2 Central Station Scenario 25

3.1.3 Cart Scenario 27

3.2 Multirotor Sizing Model 28

3.2.1 First Attempt 29

3.2.2 Final Attempt 32

3.3 Model Validation 36

4 Results and Discussion **40**

4.1 Flight-Path Model 40

4.2 Drone Sizing Model 42

5 Conclusions **48**

5.1 Achievements 48

5.2 Future Work 49

References **51**

List of Figures

1.1 Overview of CSP technologies 2

2.1 Traditional heliostat cleaning approach 8
2.2 Heliostat cleaning with HECTOR at the Gemasolar solar power plant 9
2.3 Scheme of multirotor structure 12
2.4 Flow pressure and velocity across the rotor disk 13
2.5 Momentum theory flow model 13
2.6 Blade section top view. 15
2.7 Blade cross-section. 15

3.1 Summary of model's algorithm. 21
3.2 Heliostat field layout using HelioPods. 22
3.3 STERG's HelioPod heliostat system with six mirror facets of $2.23\,\mathrm{m}^2$. 23
3.4 Multicompter's flight Scheme to transport 4 cleaning devices to the following heliostats. . 24
3.5 Different path patterns. 25
3.6 Layout and resulting outputs of 1 multirotor and 1 device. 26
3.7 Layout and resulting outputs of 1 multirotor and 2 devices. 26
3.8 Layout and resulting outputs of 1 multirotor and 4 devices. 27
3.9 Layout and resulting outputs of 1 multirotor and 2 devices plus cart. 27
3.10 Layout and resulting outputs of 1 multirotor and 4 devices plus cart. 28
3.11 $2\,\mathrm{kg}$ multirotor modeled with batteries ranging from $500\,\mathrm{mAh}$ to $14\,000\,\mathrm{mAh}$ and with propeller sizes ranging from $17\,\mathrm{in}$ to $23\,\mathrm{in}$. 29
3.12 Graphical representation of Propeller Size vs. Weight (thrust) (a & b), Propeller Size vs. Power (c & d) and Weight (thrust) vs. Power (e & f). Taken from 100 datasheets of T-motor motors [58]. 32
3.13 Linear regression line of commercial LiPo batteries. 33
3.14 $2.5\,\mathrm{kg}$ multirotor modeled with 6S batteries ranging from $1500\,\mathrm{mAh}$ to $44\,000\,\mathrm{mAh}$ with propeller sizes ranging from $19\,\mathrm{in}$ to $25\,\mathrm{in}$ and $1\,\mathrm{kg}$ payload. 35
3.15 Thrust, Power and Torque of motor MN505 K_v320 with propeller $20\,\mathrm{in}\times6\,\mathrm{in}$ found at: T-Motor [58] 36

3.16 Thrust, Power and Torque of motor MN505 K_v320 with propeller 17 in×5.8 in found at: T-Motor [58] 37
3.17 Thrust, Power and Flight-time of motor P80 K_v100 with propeller 30 in×10.5 in found at: T-Motor [58] 37
3.18 Thrust, Power and Flight-time of motor P80 K_v170 with propeller 30 in×10.5 in found at: T-Motor [58] 38
3.19 Thrust, Power and Flight-time of motor P60 K_v340 with propeller 22 in×6.6 in found at: T-Motor [58] 38
3.20 Thrust, Power and Flight-time of motor P60 K_v170 with propeller 22 in×6.6 in found at: T-Motor [58] 39

4.1 Mass of multirotor plus battery vs. flight-time of 4 kg and 4.5 kg quadrotor. 41
4.2 Flight-time for a 8.6 kg quadrotor (including payload) with batteries from 2000 mAh to 50 000 mAh and 7 propeller sizes. 42

List of Tables

4.1 Results for multirotor's path on Central Station scenario with 4 cleaning devices carrying 1 L of water each. 40
4.2 Results for multirotor's path on Cart scenario with 4 cleaning devices carrying (a) 1 L of water each (b) 0.5 L of water each. 41
4.3 Results for the reference multirotor components. 42
4.4 Diameter and pitch of the propellers plus the battery energy to attain the indicated flight-time for the all up weight (AUW) of a hovering quadcopter. RPM, power and torque, to attain the required thrust at hover, is indicated for each propeller. 43
4.5 Results for multirotor's path in Central Station scenario with 4 cleaning devices carrying 0.8 L of water each. 44
4.6 Results for multirotor's path in Cart scenario with 4 cleaning devices carrying 0.5 L of water each. 45
4.7 Specification of 7 multirotor configurations designed for 40 min flight-time and 2.8 kg payload. 45
4.8 Component summary for the chosen multirotor configuration with a 40 min flight-time . . . 45

Nomenclature

Greek symbols

α	Angle of attack.
$\ddot{\alpha}$	Angular Acceleration.
λ	Rotor Inflow Ratio.
Ω	Angular velocity.
ϕ	Velocity Inflow Angle.
ρ	Density.
σ	Solidity ratio.
θ	Pitch Angle.

Roman symbols

$\dot{m}$	Mass Flow Rate.
$\mathcal{I}$	Inertia.
A	Area.
c	Blade's cord.
E	Energy.
F	Force.
I	Current.
K_v	Rotational Speed over Input Voltage.
M	Figure of Merit.
N	Number of blades.
P	Power.
Q	Torque.

R Radius.

T Thrust.

t Time.

U Tangential Velocity.

V Axial Inflow Velocity.

w Induced Wake.

C_D Coefficient of drag.

C_L Coefficient of lift.

C_P Coefficient of power.

v Induced Velocity.

Abbreviations

ACC Air Cooling Condenser

CFD Computational Fluid Dynamics

CSP Concentrating Solar Power

DNI Direct Normal Irradiation

ESC Electronic Speed Control

GTOW Gross Take-Off Weight

HTF Heat Transfer Fluid

MDO Multi Disciplinary Optimization

MILP Mixed Integer Linear Program

PCM Phase Change Materials

PV Photovoltaic Panels

RPM Revolutions Per Minute

STERG Solar Thermal Energy Research Group

Chapter 1

Introduction

As the years pass, the world continues to face more intensely the consequences of climate change not only with higher temperatures but also with extreme climate phenomena as consequences of greater concentrations of greenhouse gases in the air. The major cause of the greenhouse gasses is the burning of fossil fuels to use as other forms of energy. Therefore, the transition to renewable energy is one of the most important actions to stop climate change. [1].

The sun shines every day and its immense power allows plants to grow, wind to blow and rain to fall which are the principal means that humans have used to produce renewable energy. Recently, humans have developed technologies to directly capture the sunlight and transform it into electric power with photovoltaic panels (PV) or Concentrated Solar Power (CSP) technologies. Utility scale CSP is a relative new type of renewable energy and its below described advantages make it an essential technology to fight climate change.

1.1 Background

1.1.1 CSP Technology

The concept of CSP is to concentrate the solar radiation on heat transfer fluid (HTF) that is then used as the heat source to produce steam and run a turbine to generate electrical power or alternatively, the heat is simply used for industrial processes. There are different types of CSP technologies. The two most commonly used technologies are the parabolic through collector technology, which uses concave mirrors to reflect the sun rays into a receiver tube, and the central receiver technology, which is a more recent technology that uses slightly curved mirrors to reflect the sun rays into a single central receiver.

In the parabolic trough technology the receiver tubes contain HTF, usually oil, that runs through the entire field constantly being heated by the concentrated reflection of the parabolic mirrors reaching temperatures of 395℃. Then the oil heats up a phase changing material (PCM), usually molten salts, located in insulated tanks which provide the thermal storage that is then use when needed to run the power block [2] as in figure 1.1(a). In the other hand, the central receiver technology uses the molten salts directly as the HTF as illustrated in 1.1(b). Significantly higher temperatures are attained by directly

employing molten salt as the HTF, consequently CSP technologies are currently transitioning form the conventional parabolic trough collector to central receiver technologies [3].

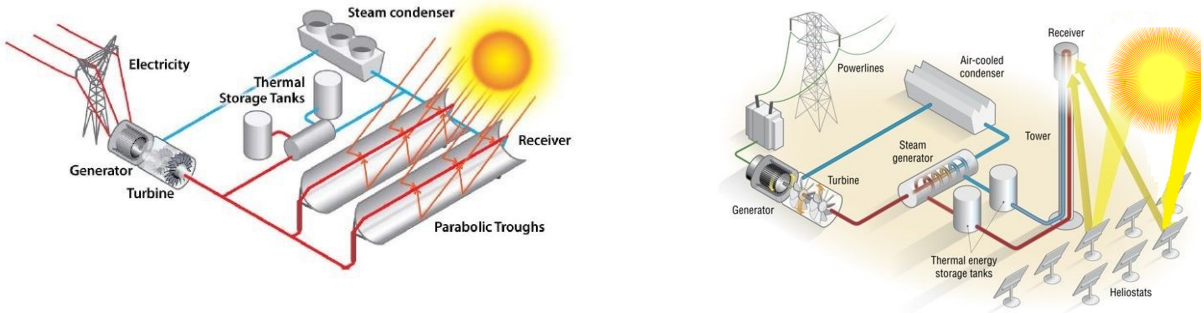

(a) Parabolic trough.

(b) Solar central receiver.

Figure 1.1: Overview of CSP technologies [4].

The problem of some renewable energy technologies such as wind and PV is that they can only produce electric power when there is wind and sun respectively, whereas the electricity demand continues regardless the weather conditions. The current solution is coupling the wind farms or PVs with batteries, but they are very costly and hazardous for the environment. In the other hand, CSP plants have the great advantage of storing the solar hours in the form of thermal storage. Thanks to the thermal storage, CSP can produce dispatchable energy that results in a great advantage over PVs and other renewable energy technologies.

1.1.2 Heliostat Cleaning

The efficiency of a CSP plant highly depends on the reflectivity of the mirrors in the heliostats [5] and therefore, it is essential to maintain the mirrors clean. The frequency on which the mirrors are cleaned depends on the ground and weather conditions. For example, the plants located in the north cape of South Africa aim to clean the mirrors every 7 days[1]. In other plants of the world, depending on the location, the mirrors require less or even more frequent cleaning. The most common technologies for washing the mirrors are cleaning vehicles [6].

The main problem of current technologies is that they use big amounts of water that are sprayed by means of hydraulic arms attached to the trucks and a slightly imprecise movements of these big arms can damage the mirrors.

CSP plants are located in high Direct Normal Irradiance (DNI) zones, which are usually desertic areas where the usage of water is a problem. This is why new technologies are starting to be implemented to reduce the consumption of water. For instance, the project MinWaterCSP is investigating to lower the elevated water consumption at the cooling towers of the power blocks by replacing the traditional technology with alternative cooling systems such as Air Cooling Condensers (ACC) or hybridized cooling, as well as technologies to minimize the water used for cleaning the mirrors by recycling the used water [7] or applying minimum water cleaning technologies.

[1] This information was given to the researcher at the technical visit of a CSP plant located in the Northern Cape, South Africa.

Another project carried by IK4 Tekniker is developing an ultrasonic cleaning system which uses small quantities of water to remove the dirt adhered to the surface of the heliostat mirror by means of a sweeping motion. Unlike other currently used cleaning techniques, such as pressurised water jets and brushes, the ultrasonic cleaning system offers significantly enhanced performance and savings in terms of water and energy resources [8].

1.1.3 UVAs for Operational and Maintenance of Solar Energy Plants

In the past years the energy sector has raised interest in using unmanned aerial vehicles (UAVs) to replace human activities of dangerous or dull nature. Currently UAVs are succesfully being used to monitor power lines, wind turbines and photovoltaic (PV) plants.

Several recent studies proposed using multirotors for PV surveillance applications to reduce the human workforce [9], including aerial thermographic inspection [10] and monitoring of PV modules to identify irregularities in the panels via infrared camera analysis [11]. Additionally, UAVs are also being considered for cleaning purposes of PV panels of large-scale plants [12]. Two technologies that propose cleaning UAVs are Solarbrush [13] which integrates a brush to the tail of a multirotor and Cleandrone [14], which uses an onboard glass cleaning device and detachable cleaning fluid container. Cleandrone also proposes the technology to be used in concentrated solar power (CSP) plants to clean the mirrors.

For CSP, very few UAV implementations were found. Essentially, UAVs are being investigated for performing inspections in real time at parabolic trough plants as a mean of detecting anomalous absorber tubes and improving the effectiveness of methodologies currently being utilized [15]. For central receiver plants, UAVs are being investigated for heliostat calibration, inspection [16] and, most recently, heliostat cleaning.

1.2 Motivation

It is necessary to reduce the amount of water used for cleaning the heliostats in CSP plants and switch to a more delicate system that does not risk to break the mirrors. At the same time, automation is key to get work done at any time avoiding the need of human labor in such remote sites. The opportunity of automating the cleaning process of heliostats by using a more delicate and water efficient technology, brings the Solar Thermal Energy Research Group (STERG) to evaluate the possibility of incorporating an ultrasonic cleaning system to a robot and create an autonomous cleaning device which will be coupled with a UAV that transports the cleaning device throughout the heliostat field. The UAV was decided by STERG together with the researcher to be a multirotor due to its relative mechanical simplicity [17].

Before the design, testing and implementation of the entire cleaning technology, STERG is willing to understanding the requirements and implications of the necessary work required to choose a multirotor, with the above assigned purpose, and have a picture of the opportunities and advantages of the technology. Therefore, the presented work focuses on framing a strategy to find the required characteristics of a multirotor whose function is to transport the cleaning device. The cleaning device itself is a separate

study carried parallel to the multirotor's study.

To accomplish the above mentioned, there is the need of a high-level model meaning a simple model that supports the understanding, analysis and decision making for the estimation of the optimal size and characteristics of the multirotor in terms of battery, propeller and motor. Such a model is not freely available and has not be found in literature as explained in Section 2.2. Therefore, this study requires to build a high-level model that can estimate the optimal configuration for a multirotor whose specific purpose is to transport the cleaning device. Additionally, a flying path for the multirotor must be modeled for a specific heliostat field to understand a suitable fly-time and quantity of water to carry.

This research fosters the implementation of automation and modern technologies necessary to add efficiency and value to CSP plants. The enhancement of CSP operations and maintenance will encourage its further development and assist to the energy transition required for a more sustainable future.

1.3 Objectives

The research is divided into two objectives which lead towards the answer to the major research question:

What are the size and specifications of the motor, propeller and battery of a multirotor whose purpose is to transport a cleaning device through a given heliostat field?

The two key objectives are:

- Design the multirotor's flying path for an example heliostat field to identify a suitable number of cleaning devices per multirotor and quantity of water needed per each device.
- Build a high-level model that can estimate the optimal drive configuration in terms of motor, propeller and battery, for a multirotor given a certain payload.

1.4 Methodology

An example heliostat field was chosen to simulate different flying paths with different amounts of cleaning devices per multirotor. The most convenient path in terms of time and multirotor's useage, was chosen to identify the amount of water needed per cleaning device which decides the payload weight. The identified payload was simulated with several motors selected from data-sheets with their recommended propeller and input voltage to find the best performing configuration in terms of flight-time.

To find the flight-time, a computer model was developed in MATLAB using Momentum Theory combined with Blade Element Theory to simulate the Thrust, Power and Torque of a multirotor with a set number of rotors a specific battery size and correspondent total weight. The model was validated by comparing the results with commercial data.

1.5 Outline

In this chapter, an overview has been stated about the question addressed in this thesis. The following chapter provides the literature review of the state of art of Heliostat Cleaning Technologies and the theory used to ground the aerodynamic concepts discussed in this paper. In chapter 3, the core model developed in this thesis work, to answer the research question, is described. The description is followed by the model's validation. Chapter 4 shows the results obtained using the model for an example case study. Lastly, the conclusions of the model and results are indicated in chapter 5 followed by the suggested future work that will enhance the current model's usefulness.

Chapter 2

Literature Review

2.1 State of Art: Heliostat Cleaning Technologies

The efficiency of CSP plants depends on the reflectance of the concentrating mirrors. Their reflectivity can be greatly reduced by soiling [18]. The dust that deposits on the heliostats influence the reflectance of the mirrors by absorbing or scattering the sun rays. The amount of dust deposited depends on its size and chemical composition as well as rain and wind which varies according to the location of the plant. In any case, the solar field performance and revenues from power-sales of CSP plants are directly related to the mirrors' reflectivity since the reduction in cleanliness corresponds to the same reduction of the overall optical efficiency of the heliostat. [19]

Mirror cleaning can restore initial reflectivity but current methods require man power, water, fuel, and maintenance as well as initial investment for the cleaning vehicles. Cleaning vehicles clean between $10.000\,\mathrm{m}^2$ and $30.000\,\mathrm{m}^2$ of mirror surface per 8 h shift and require one to two persons for operation [20]. Furthermore, if cleaning is performed during daytime, the heliostats being cleaned have to be defocused which results the thermal concentration of the solar field. Therefore, mirror cleaning is advantageous to be carried out at night time.

Mirror cleaning is part of the daily maintenance operations due to the big amount of mirror surface in the plants and the preference of cleaning each at least one once a week. For example, Helio100 is a small scale central receiver CSP plant with a nominal power of $100\,\mathrm{kW}$ and consisting of 100 heliostats, each with $2\,\mathrm{m}^2$ of mirror surface [21]. In comparison, Khi Solar One is a large scale central receiver CSP plant with a nominal power of $50\,\mathrm{MW}$ and consisting of 4000 heliostats, each with $140\,\mathrm{m}^2$ of mirror surface [22]. With the immense amount of m^2 of mirrors it is clear that the optimization and improvement of mirror cleaning is key for the performance of the field.

2.1.1 Traditional Methods

Traditional methods use water as the main cleaning agent. Pressurized air or vacuum methods are not commonly used since they result much less effective in removing dust particles than water at the same applied pressure [23]. Traditional methods are divided into non-contact cleaning and contact cleaning.

Non-contact cleaning consists of spraying high pressure water on the mirror surface. This method is acceptably efficient but does not completely remove all the cemented particles [24] [25] and the water consumtion is around $0.85\,\mathrm{L/m^2}$ [19]. A closer distance from the water nozzle to the mirror or higher water pressure will improve the dust removal [26], however the risk of touching and damaging the mirror will increase or more water will be consumed respectively.

Figure 2.1: Traditional heliostat cleaning approach using high pressure water and large hydraulic arm [19].

Contact cleaning consists of brushing or wiping the dirty surface. This method can clean the mirror up to its initial reflectance unlike non-contact cleaning methods, but it takes more time [20]. Other disadvantages are that contact cleaning can scratch the mirrors over the time and water is still needed to spray beforehand to remove loose particles [25]. Contact cleaning can be done by hand on small CSP plants that have relatively few mirrors in small sizes.

Most of the current CSP plants use the traditional cleaning methods with trucks, as shown in Figure 2.1, that have hydraulic arms and use either high pressure water or brushes with low pressure water [27]. One of the disadvantages is that an error from the operator can easily break the mirrors even though the trucks are usually equipped with sensors [6]. Other disadvantages are the deterioration of on-site roads and, as mentioned before, the high amounts of water used.

2.1.2 New Methods

Autonomous cleaning robots are being investigated as the CSP industry looks into automizing and optimizing the operations and maintenance of the plants. For example, Figure 2.2 shows HECTOR, an innovative system that can alone clean the entire heliostat with the help of an operator which distributes it along the field. Its benefits have been tested and validated. Apart from using a few liters of water to clean the entire heliostat, it cleans uniformly because of its direct contact with the surface and achieves original reflectivity of the mirror even after extreme dirty conditions. Additionally, this technology is delicate and eliminates the risk of the big cleaning trucks of breaking the mirrors. Taking into account that one

operator can manage several of these robots, this concept maximized the cleaning capacity per operator thus optimizes the plant's operations [28].

Figure 2.2: Heliostat cleaning with HECTOR at the Gemasolar solar power plant [29].

Other innovative concepts involve ultrasonic cleaning technology. This consists of using ultrasonic waves that generate cavitation bubbles that agitate the liquid producing high forces on the dust adhered to the mirror. This technology allows dust particles smaller than a micron to be removed and, compared to conventional methods, consumes 600 times less water. Moreover, this cleaning mean prevents scratching resulting from physical contact between cleaning utensils such as brushes and the mirrors as, in the long run, this reduces their reflectively irreversibly [8].

Alternatively, autonomous cleaning devices can be integrated with ultrasonic cleaning technology. Ultrasonic Cleaning applied on mirror surfaces consumes $0.03\,\mathrm{L/m^2}$ of water on a horizontal surface[1]. STERG is investigating the possibility of integrating ultrasonic cleaning system into a robot that will clean each individual mirror and will be transported around the field by means of a multirotor.

Furthermore, other investigations are done to recover the washing water. MinWaterCSP project developed an on-truck water treatment unit that recollects the used water and treats it for utilizing it again [7].

2.2 State of Art: UAVs Design Methods

Typically company specific codes are used in the industry to size rotorcrafs, otherwise, at university research level, a common method found to size large gas fueled aircraft such as man driven helicopters is the fuel fraction method (R_f) [30] [31] [32]. The method, when given a mission, provides a minimum engine size and thus attempts to size other components such as rotor blades and transmissions, as well as providing a minimum gross take-off weight (GTOW) required after calculating other component weights. However, a similar method to size electric UAV drive components was not yet found to be

[1] This information was given to the researcher by the STERG ultrasonic cleaning system developer partner.

readily available.

Magnussen [33] [34] and Dai et al. [35] address UAVs sizing using the optimization software IBM ILOG CPLEX (Cplex) in order to input the sizing variables/constraints: *Payload capacity, Dynamic performance, Flight time, Cost/complexity, Propeller RPM, Number of actuators, Propeller type, Motor type* and *Battery* (where propellers, motors and batteries are taken from datasheets) to obtain an optimal solution. Commercial solvers, such as the Cplex, outperform open source solvers since Cplex is able to optimize large scale mixed integer linear program (MILP) problems in a fast manner [36].

Other papers differentiate from optimization softwares and propose single methodologies or analytical algorithms for multirotor sizing. Gur [37] presents a multi disciplinary optimization (MDO) approach to design a propulsion system based on goals such as rate of climb and hover time, and presents a useful modeling analysis of motors and batteries as well as sensitivity analysis to certain propeller design elements. Wislow [38] identifies key driving vehicle factors implemented in a Micro Air Vehicle design tool. Starting from basic rotor parameters, such as radius, solidity, and airfoil section, and an initial gross take-off weight (GTOW), a blade element momentum theory framework coupled with computational fluid dynamics (CFD) generate an estimate of rotor power and torque for a required thrust. Gatti et al. [39] propose a revised version of a classical aircraft sizing methodology, based on statistical data available in the literature, to preliminary size an electric multirotor, taking into account mission profile and a few performance requirements. Bouabdallah [40] describes a method for iteratively designing a quadrotor with a maximum mass and length to achieve a desired thrust-to-weight ratio. The method requires a database of actuator, battery, and airframe components to calculate the loop masses. Ng et al. [41] propose a methodology with genetic algorithms to automate the component selection, layout design and geometric sizing of small-scale quadrotors. The most suitable set of components from datasheets are selected, and organize the vehicle components/payloads, such that the resulting flight vehicle has the most compact overall size without violating any given physical or mission constraint.

In contrast of most of the above mentioned researches, Bershadsky et al. [42] and Ampatis [43] propose to parameterize drive components such as motors, batteries, propellers and ESCs to rid of the need of using databases for design and optimization. Additionally, Ampatis studies the effect of varying payload on design characteristics.

Less rigorous methods in terms of optimality of UAV design also exist. For instance, eCalc [44] is a free online tool that has become one of the most popular tools for UAV hobbyists [42]. Some researches propose this tool for multirotor design [45]. eCalc allows users to input the multirotor components and outputs a calculated flight time, in addition to other useful data. eCalc requires that the specific drive components are provided to the tool. This is one of the major differences between eCalc and the analysis algorithm described in this paper. The presented model allows users to input only payload and relevant drive system parameters instead of arbitrarily selecting specific components.

2.3 Theoretical Overview of Multirotor Functionalities

Multirotors are becoming ever more common in the world of renewable energies because compared to traditional manual methods, they provide a more efficient and cost-effective system for maintaining and monitoring the conditions of the energy production plants. For instance, multirotors are being used in photovoltaic plants to detect underperforming panels [46], in wind farms to check the status, clean and defrost the rotor blades [47][48], as well as visual inspection to identify defects in power lines [49]. Multirotors can reach inaccessible areas for humans and facilitate a safe working environment. With multirotors it has become easier to carry operations and preventive maintenance. Also, multirotors allow for a faster response to system failures reducing potential impacts and downtime.
The main components of a multirotor or are:

Propellers which provide the required thrust, lift and maneuverability for the multirotor to fly. The two main specification of a multirotor's propeller are the diameter and the pitch. The number of propellers on a multirotor is usually a pair number since half of the propellers spin clock-wise and the other half spins counter-clock wise to provide optimum stability. Unlike the helicopters, multirotors do not have pitch control, the reason why maneuverability is controlled by accelerating or deaccelerating the rotation of the propellers. Most commonly, there are 2 blades per propeller, but this number can vary. The more blades, the more thrust is generated but at the same time, more losses are produced.

Motors provide the rotational power to the propellers. The most common motors used in multirotors are DC brushless motors since they are more efficient than the older brushed designs in converting electrical to mechanical energy. These come with specification such as K_v and K_t which represent the rotational speed over the input voltage and the torque over the input current respectively. One of the most important, if not the most important parameter of motor selection is the speed constant, or K_v, measured in RPM/Voltage. It is the manufacturers indication of roughly how fast the motor will spin when unloaded per applied unit of voltage. This value must be properly matched to the selection of the propeller and battery, as well as chosen for resulting efficiency and lift capability. The motor should be able to handle the mechanical and torque electrical power loads applied by turning the propeller. Too high of a K_v or voltage, and the motor may be unable to handle the loads at high throttle, or may spin in a lower efficiency regime with too low of an RPM at low throttle. Too low of a K_v and the motor may have to spin too fast to generate sufficient thrust to fly. Generaly high K_v values are used for smaller propellers that need to rotated faster to produce the same thrust in comparison with bigger propeller. In the contrary low K_v values are generally used for bigger propellers [42].

Electronic Speed Control (ESC) controls the rotational speed of the motor by providing it with the required voltage. The main parameter when selecting ESCs to consider is the maximum rated amperage. This must be sufficiently higher than the required drive current per motor such that the electronic components inside the ESC do not overheat and fail.

Battery supplies the energy required from the motors and ESC. The most common batteries used for multirotors are the LiPo with specific energy of up to around 250 Wh/kg [50]. The main specification of these batteries are the voltage that results from the amount of cells in series (each cell has a maximum

voltage of 4.2 V and a minimum voltage of 3.2 V hence, the calculations in the model assume the average value of 3.7 V). The capacity, normally measured in mAh, determines the energy storage of the battery. A 1000 mAh battery can provide 1A of current for 1 hour if 100% discharged. The discharge rate, specified as "C-rating" of a battery, is a manufacturer's indication of the discharge capability of the battery. The C-Rate of a battery times the capacity determines the maximum current, I, that a battery can give for a certain time. For example: A 20C 1000 mAh battery in an operational condition is capable of sustaining 20A discharge for 3 minutes. The power requirements of the drive system must be taken into account when selecting the battery. In the present work, the recharge rate is assumed to be 1 C for all the modeled batteries, meaning they will fully recharge in 1 hour.

Figure 2.3 summarizes the electric propulsion system of a multirotor, where P_{IN} ($V_{\mathrm{BATT}} \times I_{\mathrm{BATT}}$) is the electrical power provided by the battery to power the ESC and the motor which converts the electrical power into a torque (Q) at an angular velocity (ω) which then the propeller converts into an aerodynamic thrust (T).

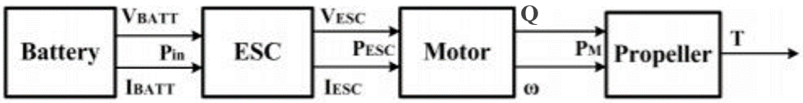

Figure 2.3: Scheme of multirotor structure [51].

Frame holds the drive system together, as well as the **Flight Control** and the **Cabling**.

2.4 Aerodynamics

2.4.1 Momentum Theory

Momentum theory uses the fundamental laws of fluid mechanics (conservation of mass, energy and momentum), to relate the inflow and outflow of the propeller's plane to its thrust and power. The model is useful to understand the global mechanism of the rotor including the limits for an ideal performance and the induced power requirements, but it is not enough to physically design a propeller since it does not relate to the loads or flow around the blades [52].

To use momentum theory, the rotor is assumed to be a disk of infinite amount of blades which adds momentum and energy to the air flow. The rotor can accelerate the air flow downstream thanks to the pressure difference that it can support across it as shown in Figure 2.4, in this way produces thrust in the opposite direction of the downstream air.

Figure 2.5 shows the axial inflow velocity which the rotor experiences during horizontal or vertical flight where V is the velocity at which the rotor is moving, v is the induced velocity of the air generated by the rotor and w is the wake or induced velocity at far downstream.

Momentum theory assumes that:

- The propeller has a steady load across its surface.

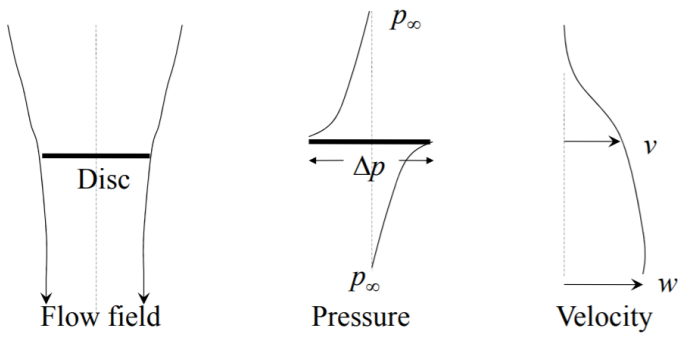

Figure 2.4: Flow pressure and velocity across the rotor disk [52].

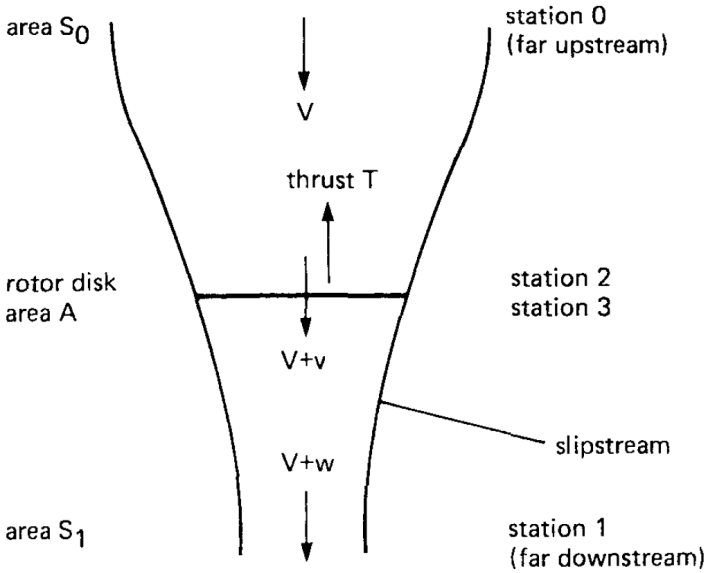

Figure 2.5: Momentum theory flow model [53].

- The swirl in the wake due to the rotor's torque is neglected.
- The induced velocity, v, and induced wake, w, is uniform over the slipstream and far downstream respectively (Figure 2.5).
- The fluid is incompressible.
- Flow is steady and inviscid.

Refering to Figure 2.5, the mass flux through the propeller disk if given by:

$$\dot{m} = \rho A(V + v) \tag{2.1}$$

where $\dot{m}$ is the mass flow of the air through the rotor's disk, ρ is the air density and A is the surface area of the rotor's disk. Momentum conservation states that the momentum at Station 3 minus momentum at Station 0 equals the thrust generated at Station 2.

$$T = \dot{m}(V + w) - \dot{m}V = \dot{m}w \tag{2.2}$$

Conservation of energy states that the kinetic energy at Station 3 minus kinetic energy at Station 0 equals the work generated at Station 2.

$$T(V+v) = \frac{1}{2}\dot{m}(V+w)^2 - \frac{1}{2}\dot{m}V^2 = \frac{1}{2}\dot{m}w(2V+w) \tag{2.3}$$

Solving for the induced wake $T/\dot{m}$ in Eq. (2.2) and Eq. (2.3) results in $w = 2v$. Therefore, the new thrust relation can then be expressed as:

$$T = \dot{m}w = 2\rho A(V+v)v \tag{2.4}$$

At hover conditions the rotor has no forward or vertical speed so $V = 0$. Thrust generated at hover is then expressed as:

$$T = 2\rho A v^2 \tag{2.5}$$

Solving for the induced velocity at hover yields:

$$v_{\mathrm{h}} = \sqrt{\frac{T}{2\rho A}} \tag{2.6}$$

The ideal induced power required to hover can then be determined for a given thrust:

$$P = Tv_{\mathrm{h}} = T\sqrt{\frac{T}{2\rho A}} \tag{2.7}$$

2.4.2 Blade Element Theory

Blade Element Theory comes closer to the blade's reality unlike Momentum Theory that considers the propeller as a disk composed of infinite amount of blades, and who's surface produces a pressure jump. Blade Element Theory is used to calculate the interaction with the fluid over each section of the blade which then is integrated to find the resultant forces over the entire blade [54].

Figure 2.6 is the top view of a rotor where R is the radius, y is the radial length ($y = 0$ at the hub and $y = R$ at the tip), c is the blade's cord, Ω is the angular velocity and ΩR is the tangential velocity.

Figures 2.7 is the profile view of a blade. The blade section pitch, θ, is measured between the plane of rotation and the zero lift line. The aerodynamic angle of attack, α, is measure between the resultant air velocity seen by the blade, U, and the zero lift line and can be expressed as $\alpha = \theta - \phi$. U has a tangential component, $U_T = \omega y$, and a perpendicular component, $U_P = V + v$.

The resultant velocity inflow angle can be given by:

$$\phi = arctan\left(\frac{U_{\mathrm{P}}}{U_{\mathrm{T}}}\right)$$

The rotor inflow ratio, λ, defined as the ration of the total inflow velocity to the rotor tip speed $\lambda = (V+v)/(\Omega R)$ (the inverse of tip speed ratio for wind turbines). Inflow ratio at hover can be written in terms of thrust and angular velocity:

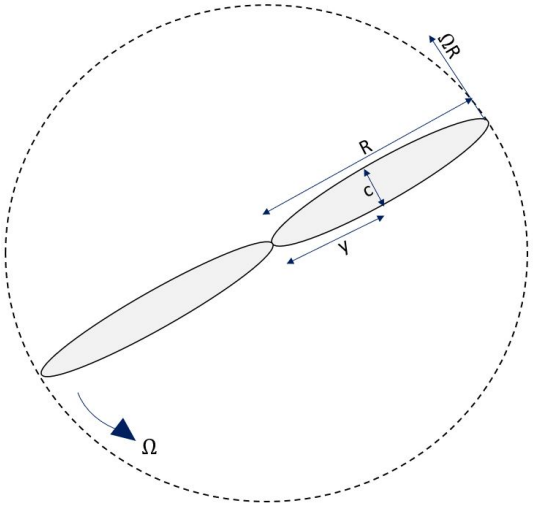

Figure 2.6: Blade section top view.

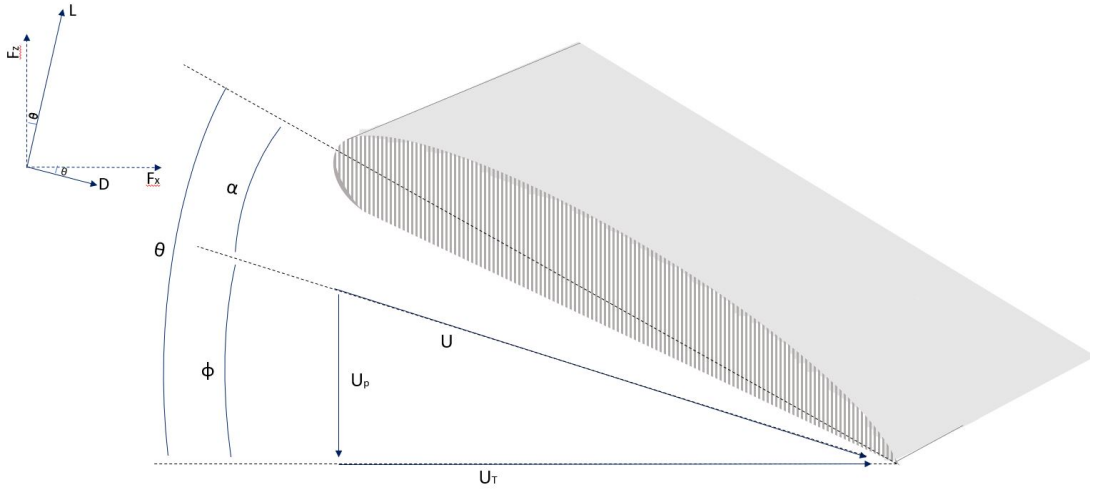

Figure 2.7: Blade cross-section.

$$\lambda_{\mathrm{h}} = \frac{\sqrt{\frac{T}{2\rho A}}}{\Omega R} \tag{2.8}$$

The section lift force,L, and drag force, D, act normal and parallel to the resultant velocity vector, U, respectively. The section lift and drag forces are expressed as:

$$L = \frac{1}{2} c \rho U^2 c_l \tag{2.9}$$

$$D = \frac{1}{2} c \rho U^2 c_d \tag{2.10}$$

where c is the blade chord, ρ is the air density and c_L and c_D are the section lift and drag coefficients respectively.

c_l and c_d are complicated functions of the angle of attack, α. To simplify calculation of c_l, the stall and compressible effects are assumed to be negligible so that c_l can be expressed as a linear relationship

between the section lift coefficient and the angle of attack, $c_l = a\alpha$ [55], where a is the slope of the blade two-dimensional lift curve and is denoted by $a = 5.7$ as a typical value used in literature [53].

From the diagram on the top left corner of Figure 2.7. The force acting on the x and z direction of the blade are given by:

$$F_z = Lcos(\phi) - Dsin(\phi) \tag{2.11}$$

$$F_x = Lsin(\phi) - Dcos(\phi) \tag{2.12}$$

Defining the differential thrust, torque and power with the acting forces on the blade section and multiplying times the number of blades, N, results in:

$$dT = NF_z dr \tag{2.13}$$

$$dQ = NF_x r dr \tag{2.14}$$

$$dP = \Omega dQ = \Omega NF_x r dr \tag{2.15}$$

The total forces on the propeller are obtained by integrating from the root to the tip of the blades.

It is assumed that the rotor has a low disk loading, meaning the inflow velocity of λ is small compared to the rotational speed, and consequently, U_P/U_T is also small. This is a reasonable assumption as the rotor operates at high angular velocities. Therefore, small angle assumption, $\phi = arctan(U_P/U_T) \ll 1$, is applicable to the propeller of a multirotor and it approximates $\phi \simeq U_P/U_T$, $cos(\phi) \simeq 1$ and $sin(\phi) \simeq \phi$. With the application of small angle theory, the blade section forces and the differential thrust and torque are reduced to:

$$L \simeq \frac{1}{2} c\rho U_T^2 a(\theta - U_P/U_T) \tag{2.16}$$

$$D \simeq \frac{1}{2} c\rho U_T^2 c_d \tag{2.17}$$

$$dT \simeq NLdr \tag{2.18}$$

$$dQ \simeq N(L\phi + D)dr \tag{2.19}$$

Defining as coefficients the ratios between the actual thrust, torque and power obtained from the propeller and the respective theoretical that the air would have over the entire disk area and angular velocity, results in:

$$C_T = T/[\rho A(\Omega R)^2] \tag{2.20}$$

$$C_Q = Q/[\rho A(\Omega R)^2 R] \tag{2.21}$$

$$C_P = P/[\rho A(\Omega R)^3] \tag{2.22}$$

Using the definition of dT in equation 2.18 the differential C_T can be explained as:

$$dC_T = \frac{\sigma a}{2}(\theta r^2 - \lambda r)dr \quad \text{with} \quad \sigma = \frac{N}{\pi R^2}\int_0^R c(r)dr \tag{2.23}$$

Where $r = y/R$ and represents a Dimensionless radial location on the blade, measured from the

hub, $r = 0$, to the blade tip, $r = 1$. From Eq. 2.19 the differential torque depends on the drag that is approximated using the drag coefficient c_d. Unlike c_L, c_d cannot be easily simplified. Using the theoretical definition, Power can be defined as $P = \Omega Q$ and from Eq. 2.21 and Eq. 2.22, the toque coefficient is assumed to be equal to power coefficient, $C_P = C_Q$ [53].

From figures 2.6 and 2.7: $U_p/U_t = (V + v)/\Omega y = \lambda(R/y)$. Taking into account that for an ideal blade with ideal distribution, $\theta = \theta_t/r$ [53], where θ_t is the pitch angle at the tip of the blade, equation 2.23 results in:

$$C_T = \frac{\sigma a}{4}\alpha_t \tag{2.24}$$

From Eq. 2.8 and Eq. 2.20 the rotor inflow ratio at hover can be expressed in terms of C_T.

$$\lambda_{\mathrm{h}} = \sqrt{\frac{C_T}{2}} \tag{2.25}$$

Substituting Eq. 2.22 with C_t and λ_h results in:

$$C_P = C_T\lambda = \frac{C_T^{\frac{3}{2}}}{\sqrt{2}} \tag{2.26}$$

The C_P for an ideal blade only represents the induced power loss. A real blade has the additional power losses listed below with the respective share out of the total power loss [53].

1. Induced power 60%
2. Profile power 30%
3. Nonuniform inflow 5% to 7%
4. Swirl in the wake less than 1%
5. Tip losses 2% to 4%

From Figure 2.7 $\theta = \alpha + \phi$ therefore,

$$\theta_t = \frac{4C_T}{\sigma a} + \lambda \tag{2.27}$$

Solving for the rotor inflow ratio results in:

$$\lambda = -\frac{\sigma a}{8} + \frac{1}{2}\sqrt{\left(\frac{\sigma a}{8}\right)^2 + 4\frac{\sigma a}{8}\theta_t} \tag{2.28}$$

2.4.3 Figure of Merit

Figure of merit is defined as the ideal power loss over the actual power loss of the propeller [56].

$$M = \frac{P_{\mathrm{ideal}}}{P} = \frac{T\sqrt{\frac{T}{2\rho A}}}{P} \tag{2.29}$$

According to literature, at the design loading of the rotor, the typical figure of merit, M, lays in between 0.55 and 0.60 [53]. $M = 0.6$ was used in the model below to estimate the real performance of a propeller.

Chapter 3

Modeling

The model is divided into two submodels that depend on each other's outputs to define the inputs.

The first model is the Flight-Path model. The Flight-Path model builds an example heliostat field from which different flying paths are simulated with different amounts of cleaning devices per multirotor. The path accomplished in the least amount of time and also requiring the least airborne and idle time for the multirotor is chosen to identify the main design requirements of the multirotor and cleaning device. For this case study the amount of water fitted into the cleaning device needs to be identified to then be given to the cleaning device manufacturer (it is only to be considered the manufacturer's suggestions of keeping the water amount among 1-3 L range). The weight of the water plus the cleaning device would equal the weight of the multirotor's payload.

The weight of the payload is used in the second model, the Multirotor Sizing model, to be simulated with several motors taken from the data sheets of the multirotor motor manufacturer, T-motor. 100 different motors where selected with the suggested propellers and input voltage. Then each motor plus propeller configuration was simulated with 50 different battery sizes plus the selected payload to obtain the flight-time. The configuration with the longest average flight-time, with all battery sizes, is then chosen as the reference multirotor configuration.

In the last part, the reference configuration is set to achieve certain flight-times. For each set flight-time the model outputs the battery required and other parameters such as constant RPM, power and torque which relates to the inertia and the maneuverability of the multirotor. The user can then choose the most suitable multirotor configuration that results in a respective flight-time.

The summary of the iterative model is displayed below in figure 3.1. The graphic summarizes the flow algorithm of the two submodels who's inputs and variables depend on each other.

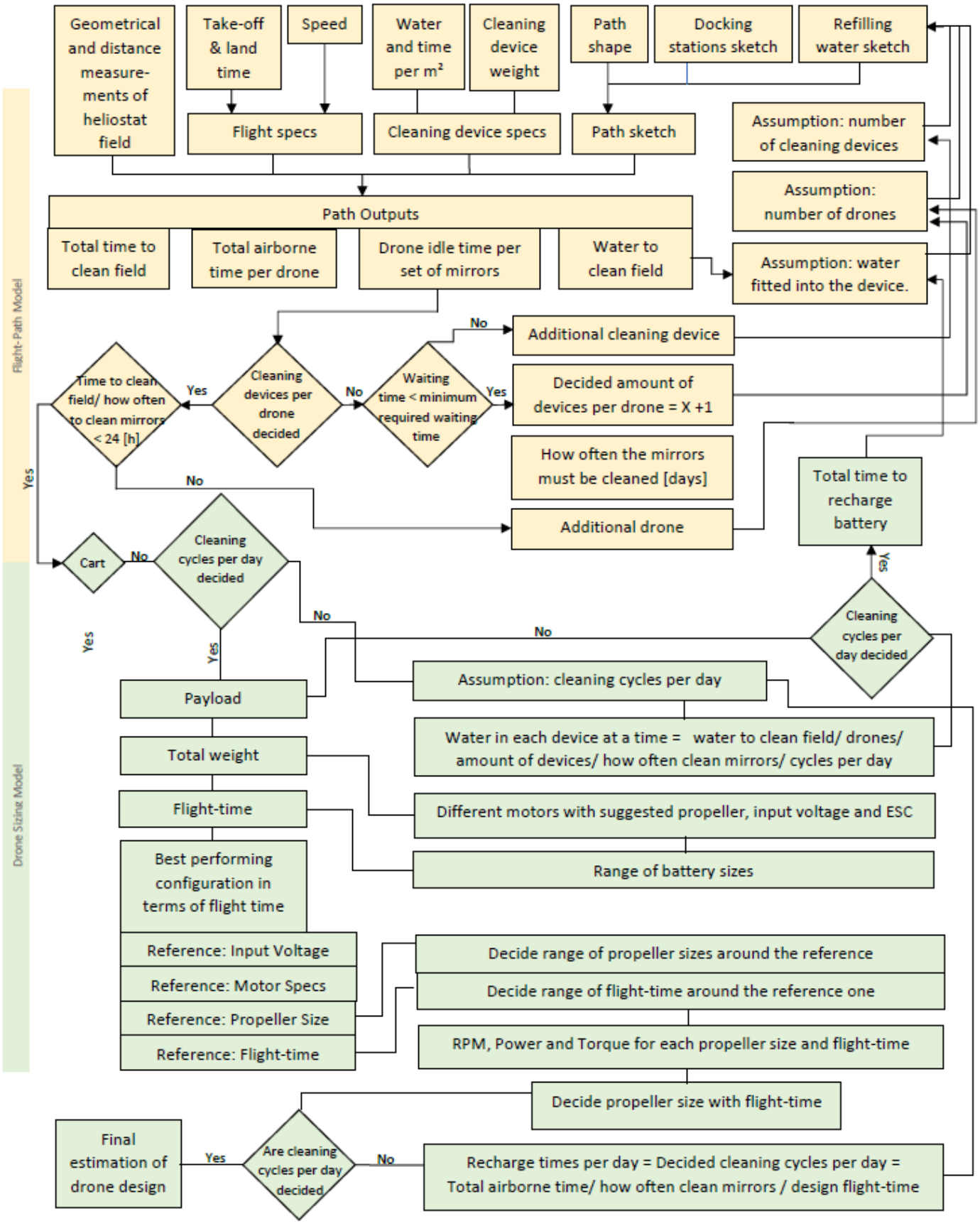

Figure 3.1: Summary of model's algorithm.

3.1 Flight-Path Model

The heliostat field should be circularly shaped around the tower to minimize the distance and optimize field performance. An analysis comprising the study of an optimal heliostat field disposition includes: (1) optimizing the distance in between the different heliostat rows to minimize blockage and (2) find the trade-off between heliostats at a closer radial distance from the tower along a longer circumference section or heliostats at a longer radial distance within a shorter circumference section. For an analysys including optimal heliostat field disposition, the space from heliostat to heliostat and from heliostat to tower should be assigned with polar coordinates to accurately calculate the distances and flight-times. However, the presented work does not include the optimization of the heliostat field layout. Therefore, for simplicity of the calculations, it is assumed that the field has a rectangular shape facing the tower with an equal distance in between heliostats rows depending on the below described HelioPod dimensions.

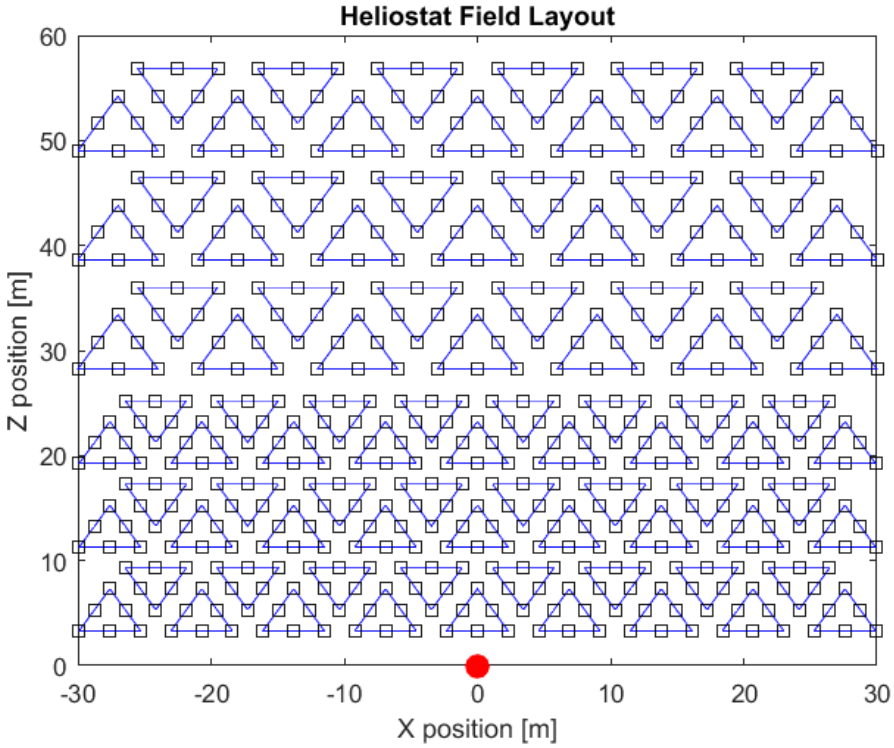

Figure 3.2: Heliostat field layout using HelioPods.

STERG works with a modular structures that hold 6 heliostats together in a triangular layout as in Figure 3.3. Such a system is referred to as HelioPod and its purpose is to lower the installation costs. The triangular shape allows to have the same distance from mirror to mirror while maintaining an open window in front of the mirrors to avoid blockage of the sun rays reflection. The heliostat field is composed by HelioPods with two different side lengths: the HelioPods located farther from the tower are bigger and have a longer separation distance, compared to those closer to the tower, to avoid blocking the reflection of the sun rays. In Figure 3.2, the black squares represent the heliostats and the triangle of heliostats represent the HelioPod pedestal.

The model allows to change the number of heliostats per row and the number of heliostat rows. This

means that it is possible to input HelioPods with less than 6 heliostats. The size of the mirrors, the size of the HelioPod structure and the distance in between the HelioPods can be changed as desired.

Figure 3.3: STERG's HelioPod heliostat system with six mirror facets of $2.23\,\mathrm{m}^2$ [20].

The location of the heliostat field was set to be in the Northern Cape of South Africa, one of the zones with highest DNI in the world. The example heliostat field has 540 heliostats, each one with the standard HelioPod mirror area of $2.23\,\mathrm{m}^2$. The smaller HelioPods have equilateral sides of $4.6\,\mathrm{m}$ length and the the bigger HelioPods have equilateral side of $6\,\mathrm{m}$ length. In general, the example field is not a large heliostat field compared to other ones in South Africa that have over 4000 mirrors, each one with an area of $140\,\mathrm{m}^2$ [22].

3.1.1 Outputs and Inputs

The outputs of the model are then used to decide the amount of multirotors, the amount of cleaning devices per multirotor, the cleaning cycles per day and the amount of water to fit in each device. The four outputs are listed below with the required fixed inputs.

1. Total water needed per cleaning device. This is known by calculating the total water needed to clean the field ($36\,\mathrm{L}$) that results from multiplying the water needed to clean each of the 540 mirrors ($0.067\,\mathrm{L}$) times the number of heliostats.

2. The total airborne time. This is the sum of all the distances that the multirotor flies to transport the cleaning devices from heliostat to heliostat, the traveled distance to dock and the traveled distance to refill the water and charge the battery. The total traveled distance is divided by the assumed average multirotor speed ($3\,\mathrm{m/s}$) plus the sum of all the times that it took-off or landed (the time to take-off/land is assumed to be 10 seconds to count a margin for the extra energy required for takeoff).

3. Multirotor idle time. This is the time that the multicopter has to wait while all cleaning devices are done with the respective heliostat. For instance, in Figure 3.4 the numbered arrows indicate the order in which the moves are performed and the broom icons represent the cleaning device. The yellow arrows indicate the movement to transport the cleaning devices and the red lines represent the movement to the docking heliostat. The multicopter has to do movement *2* and *3* to pick up the 1^{st} cleaning device, then do movement *4* and *5* to pick up and place the 2^{nd} device and so on until all four devices are piked up and placed in the following heliostats. After placing the 4^{th}

cleaning device, the multicopter does movement *10* to dock and wait for the 1^{st} cleaning device to be done. This last waiting time is defined as the Multirotor Idle Time. Idle time is equal to the time it takes the first placed device to clean the mirror ($3\,\text{min}$ and $36\,\text{s}$) minus the time required to pick up all other devices and place them in the next mirrors.

4. Total time to clean the field. This is the sum of airborne time, idle time and battery charging time.

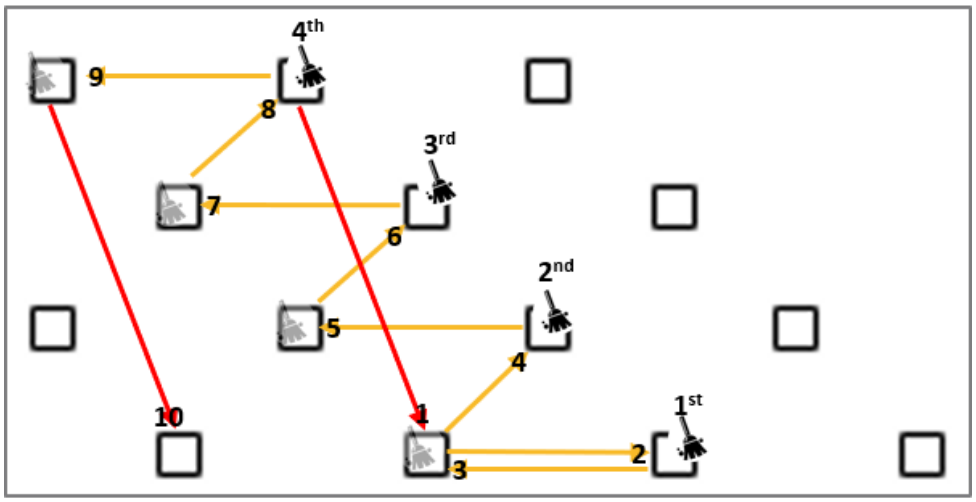

Figure 3.4: Multicompter's flight Scheme to transport 4 cleaning devices to the following heliostats.

To obtain the above-mentioned outputs, the entire path sketch has to be designed which comprises (1) selection from different path patterns of the multirotor to identify the one with less flight-time, (2) docking spots while the multirotor waits for the device(s) to finish cleaning and (3) the path for water refilling and battery charging. To design the three mentioned components, some input variables have to be defined through an iterative process. In the first iteration their value is an assumption that is then adjusted based on the results obtained afterwards. The three iterative variables are:

1. Number of multirotors. This is defined dividing the total time to clean the field into how often the mirrors should be cleaned according to the plant's requirement. Since this example field has no plant requirements, 7 days were considered because it is the standard time for the plants located in the Northern Cape of South Africa[1].

2. Number of cleaning devices. The multirotor is found to be significantly more expensive than the cleaning device, therefore, it is required to find the most amount of cleaning devices that the multirotor can handle at a time to optimize the multirotor's usage and value.The first assumption is 1 device to then continue adding devices until the waiting time of the multirotor is as close as possible to 1 minute but never less than $1\,\text{min}$ since this is the assigned buffer time. The devices are incremented one by one so that the advantages and consequences of adding an extra device are clear.

3. Water fitted into the device at a time. The fist assumption is $1\,\text{L}$. Then, the ideal is to adjust the quantity of water so that refilling of the water matches with the multirotor's battery recharging to do

[1] This information was given to the researcher at the technical visit of the CSP plants in the Northern Cape of South Africa.

only one trip and optimize the flight-path. The times required to recharge the battery each day is the final output of the multirotor sizing model and determines how many cleaning cycles are done per day (one cleaning cycle lasts as long as the battery last). Dividing the amount of mirrors that each device has to clean every day into the cleaning cycles per day results in the amount of water fitted into the device at a time.

Different flight patterns where modeled to find the one that travels the less distance to distribute the cleaning devices. The two best resulting patterns are shown in Figure 3.5. The two patterns where modeled for 2, 3 and 4 devices. As the number of devices increased, pattern (b) resulted in considerably less distance traveled, thus this pattern is selected as the standard pattern to use in the rest of the model. In Figure 3.5 and all other path sketches shown below, the yellow lines represent the flight trajectory to pick up and place the cleaning devices and the red lines represent the flight trajectory to dock.

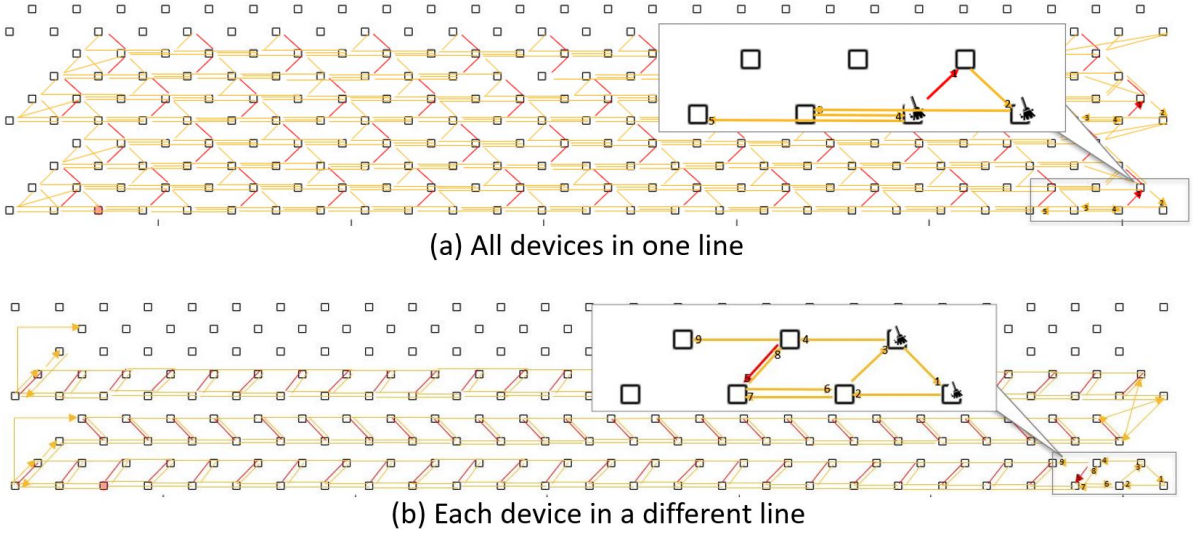

Figure 3.5: Different path patterns.

The longest flight distance carried by the multirotor is from the heliostat to the central tower to either refill the water or charge the battery. To reduce this travel distance either a water and battery recharge station can be placed in specific points of the field or an autonomous cart could carry the water to refill the cleaning devices. In this study the two most different options were considered: (1) having the multirotor travel each time to the central station and (2) having an autonomous cart next the multirotor to recharge the water. Comparing the two most different option will allow the understanding of the benefits of reducing the flight distances for recharging. Considering the above, two scenarios were defined (1) Central Station scenario (2) Cart Scenario. At this point of the model, the scenarios do not consider the time to charge the battery or refill the water.

3.1.2 Central Station Scenario

In the Central Station Scenario, the multirotor brings back to a central station the cleaning devices when it is needed to refill them with water and ideally recharge the multirotor's battery as well.

The bottleneck of the path is the amount of time that it takes the device to clean each mirror (3 min and 36 s). Assigning more devices to the same multirotor alleviates the bottleneck although the path sketch gets more complicated. More than 4 devices was not further considered since the fifth device resulted on a waiting time of less than the 1 minute required buffer.

The figures below shown the paths with the flying, docking and recharging sketch for one multirotor carrying one, two and four devices. The figures only show the path over the first rows of the field as this is enough to understand the pattern. The green lines represent the flight trajectories to refill the water and recharge the battery. The box, in the left side, displays the outputs of the respective layout. The box in the right side is a zoom-up of the of the flying pattern. The red and yellow lines as well as the numbered arrows and cleaning devices have the same meaning as in Figure 3.4

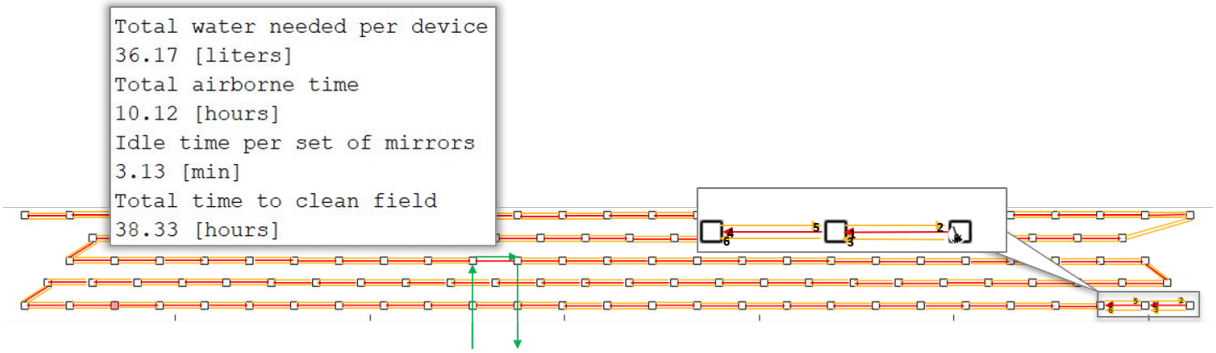

Figure 3.6: Layout and resulting outputs of 1 multirotor and 1 device.

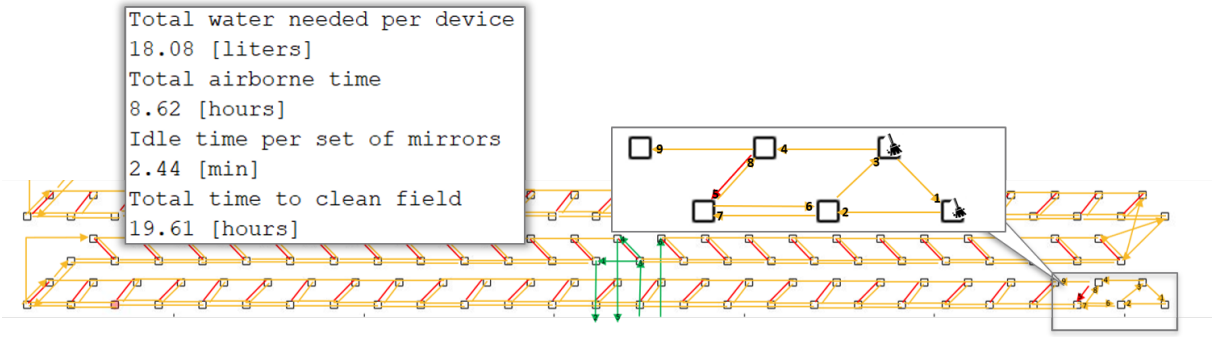

Figure 3.7: Layout and resulting outputs of 1 multirotor and 2 devices.

From the Figures 3.6, 3.7, 3.8 it is found that each additional device reduces the total cleaning time by almost its respective percentage of total devices. For instance, total time to clean the field with two devices takes almost half the time that it takes with one device and total time to clean field with four devices takes almost half the time that it takes with two devices. Additionally, the total airborne time is also reduced since the multirotor has to dock less times per mirror and the waiting time is also decreased.

It is desired to utilize the multirotor as much as possible avoiding it to be idle, but at the same time, never allowing the devices to wait for the multirotor to pick them up since this situation would add to the bottleneck. To avoid this to happen, it is appointed a buffer time of 1 minute for the multirotor to

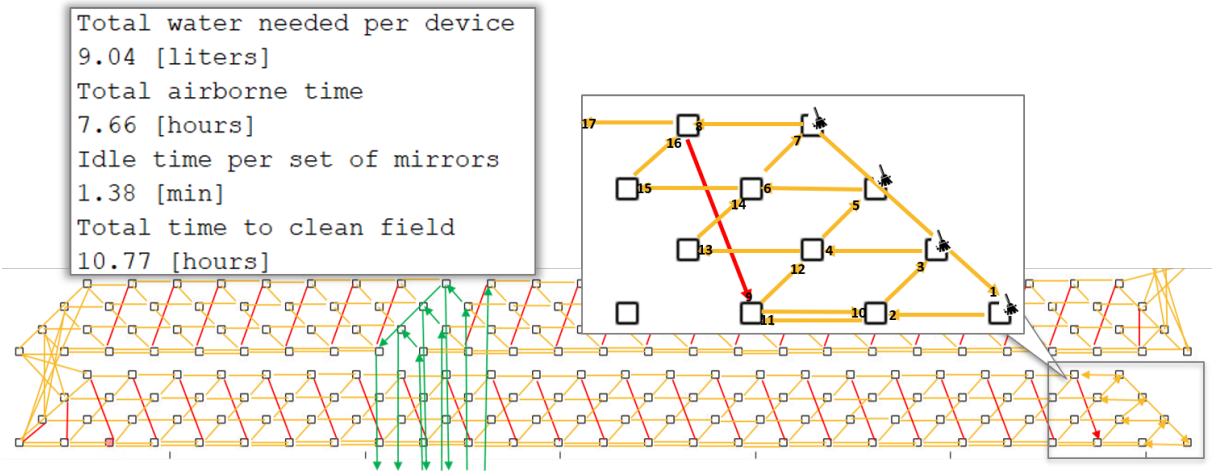

Figure 3.8: Layout and resulting outputs of 1 multirotor and 4 devices.

wait. During the waiting time the multirotor can also do some inspection on the heliostats for calibration purposes. In case the waiting time is decided to be less than 1 minute, it could be beneficial to evaluate the possibility of leaving the multirotor airborne instead of docking it due to the higher consumption of energy when taking off [57].

3.1.3 Cart Scenario

In the Cart Scenario the multirotor takes the devices to the cart when it is time to refill the water and docks at the cart assuming that the multirotor can land in a platform placed on top of the cart aligned at the heliostat level in flat position. It is assumed that the cart is able to perform navigation and localization and can park next to the heliostat that has operating the cleaning device that is being picked up after the waiting time. The ground vehicles such as the cart or the cleaning device have a much longer battery duration compared to that of the multirotors. Thus, the recharging of the battery in the cleaning device and the cart is not considered in the model.

The figures below shown the paths with the flying, docking and water recharging sketch for one multirotor carrying two and four devices with the respective output results.

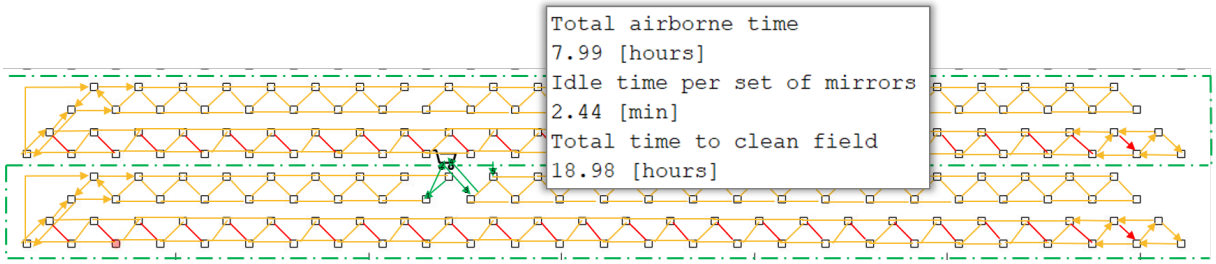

Figure 3.9: Layout and resulting outputs of 1 multirotor and 2 devices plus cart.

The Cart scenario reduces the *Total Airborne Time* and consequently reduces by the same amount the *Total Time to Clean the Field* because removes the trip to return to the central station for water refiling and, after docking, it does not have to fly back each time to pick up the device.

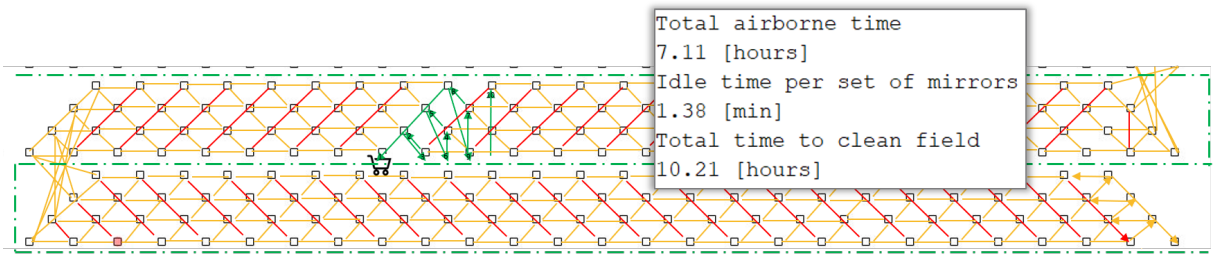

Figure 3.10: Layout and resulting outputs of 1 multirotor and 4 devices plus cart.

3.2 Multirotor Sizing Model

The purpose of the multirotor sizing model is to find an estimate of the most appropriate propulsion system combination meaning propeller and battery size with a suitable motor so that the multirotor can make an optimal performance on a given heliostat field in terms of flight time and payload capacity.

The model uses momentum theory combined with blade element theory to simulate the Thrust, Power and Torque of a propeller with a given pitch angle that depends on the propeller size. The results where validated by comparing them with data sheets of commercial motors with propellers.

The model allows to insert multicopters with as many rotors as decided. For the first strategy study, it was decided to model a quadcopter (multirotor with 4 motors and 4 propellers) since it represents the simplest configuration and gives a valid idea of the studied scenarios. The presented outcomes in this work are only the results of modeling a quadcopter.

For the purpose of the multirotor, it is desired to have the longest flight-time. One way to increase the flight-time is using longer propellers. Increasing the propeller's radius is generally more efficient, assuming the rest of the drive system meaning motor, battery and ESC, is capable of handling the load. This is because the larger propeller, with all else being equal, may spin slower to generate the same lift. This allows the induced velocity to drop, thereby increasing propulsive efficiency [42]. However, there is a technical limit with the propeller size ans the motor used, thus for bigger propellers a bigger motor is required but at the same time a bigger motor withdraws more current from the battery which reduces flight-time. Another way to increase the flight-time is with a bigger battery in terms of energy [mAh]. With more energy the multirotor can fly longer but at the same time, the increase in battery's energy is proportional to the increase in weight and a heavier weight requires more power from the motors which again, reduces flight-time. Figure 3.11 shows the typical curve that relates total mass of the multirotor and the flight-time where the x-axis represents the multirotor's weight with different sizes of battery that result in different total weights and the y-axis represents the flight-time for the specific multirotor and battery which is obtained as explained in section 3.2.2. The graph is repeated for different propeller sizes to illustrate how bigger propellers attain longer flight-times.

Although the mathematical model used will always give a longer flight-time for a bigger propeller, in reality, the motor's power and electrical constraints, limit the propeller size.

At present, there is limited understanding of how to accurately size a multirotor's drive system for a specific purpose. However, empirical relationships may be derived for these components based on manufacturer data. The two different approaches explained below were executed in the attempt to find

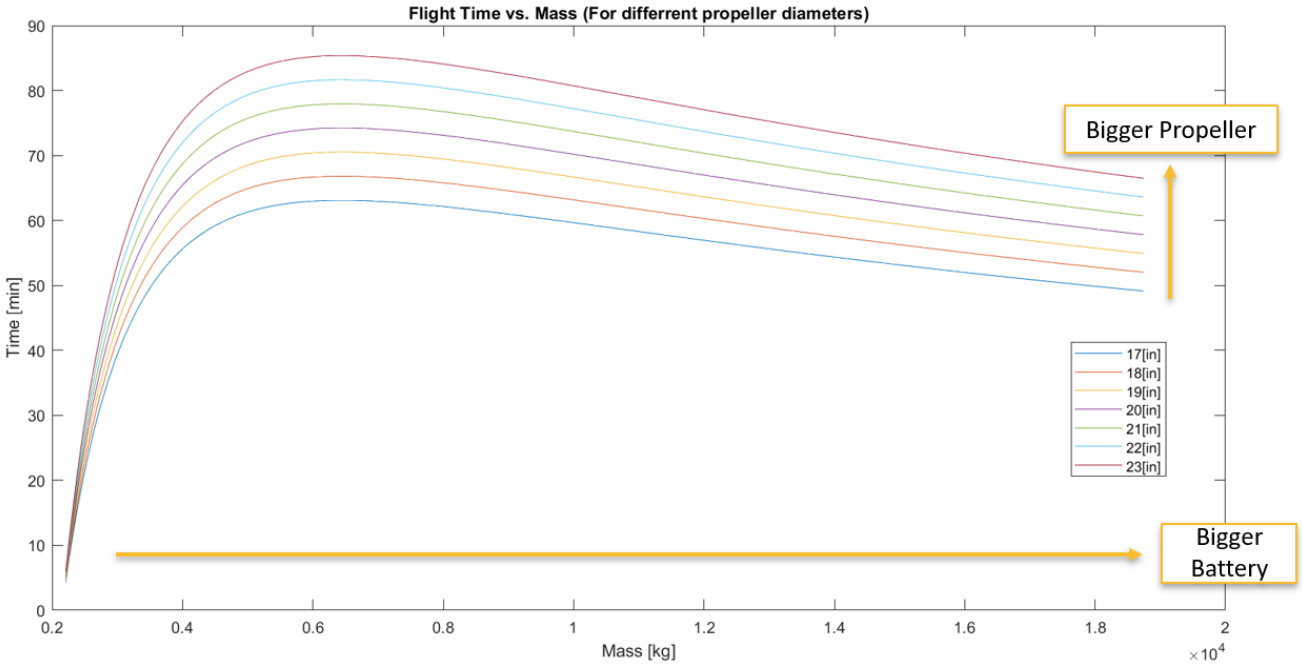

Figure 3.11: 2 kg multirotor modeled with batteries ranging from 500 mAh to 14 000 mAh and with propeller sizes ranging from 17 in to 23 in.

a multirotor sizing solution within the practical motor/propeller constraints.

3.2.1 First Attempt

The data sheets of a multirotor manufacturer were analyzed in the attempt to understand the limitations of the propeller size [58]. T-motor is a UAV motor manufacturer that also produces propellers, ESCs, frames, flight controllers and entire multirotors. This manufacturer provides the motor specifications with the suggested propeller size, ESC and input voltage. Considered a complete and reliable manufacturer, it was decided to analyze the data sheets of 100 different motors plus the respective suggested propellers of T-motor.

The propeller size, maximum thrust and power at 100% throttle was graphed to understand the relation that the manufacture experts use between multirotor's weight and propeller size. Figure 3.12 shows the relation between (a) propeller size and weight, (c) propeller size and power and (e) weight and power. The color bar on the right refers to the color of the dots that represent the current in ampers, A, required by the motor for the respective thrust or power.

There is a clear relation between weight, or in other words the thrust generated, and the power required by the motor since power depends on the thrust and the rotational velocity. In the other hand, the relations between propeller size and weight or propeller size and power is not clear, specially for propeller sizes between 25 in and 33 in. To enhance the analysis of the relations of the weight with the propeller size, the K_v of the motor was added as shown in (b), (d) and (f).

From the resultant graphs it can only be concluded that: (1) In general, a bigger propeller results

in higher thrust and power due to the bigger rotational disk area; (2) motors with higher K_v are used for smaller propellers which require less power. However, it is not possible to determine a clear correlation between propeller size and thrust or weight of the multirotor, specially for propeller in the size range of 25 in - 33 in therefore, this approach was not useful to establish a correlation between the drive components of commercial multirotors.

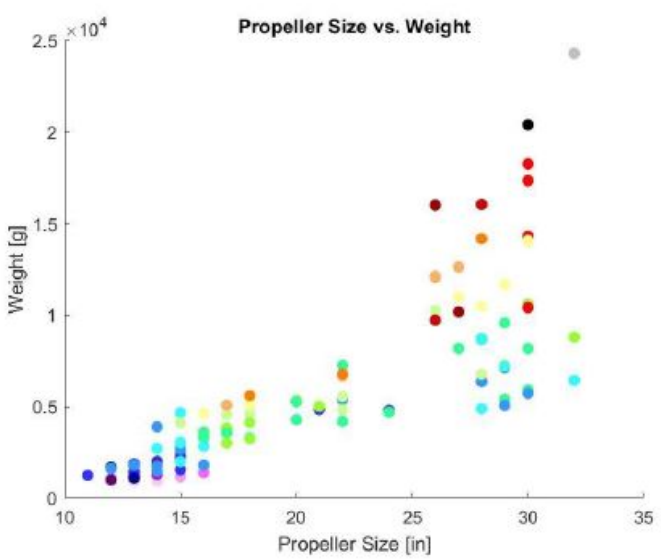

(a)

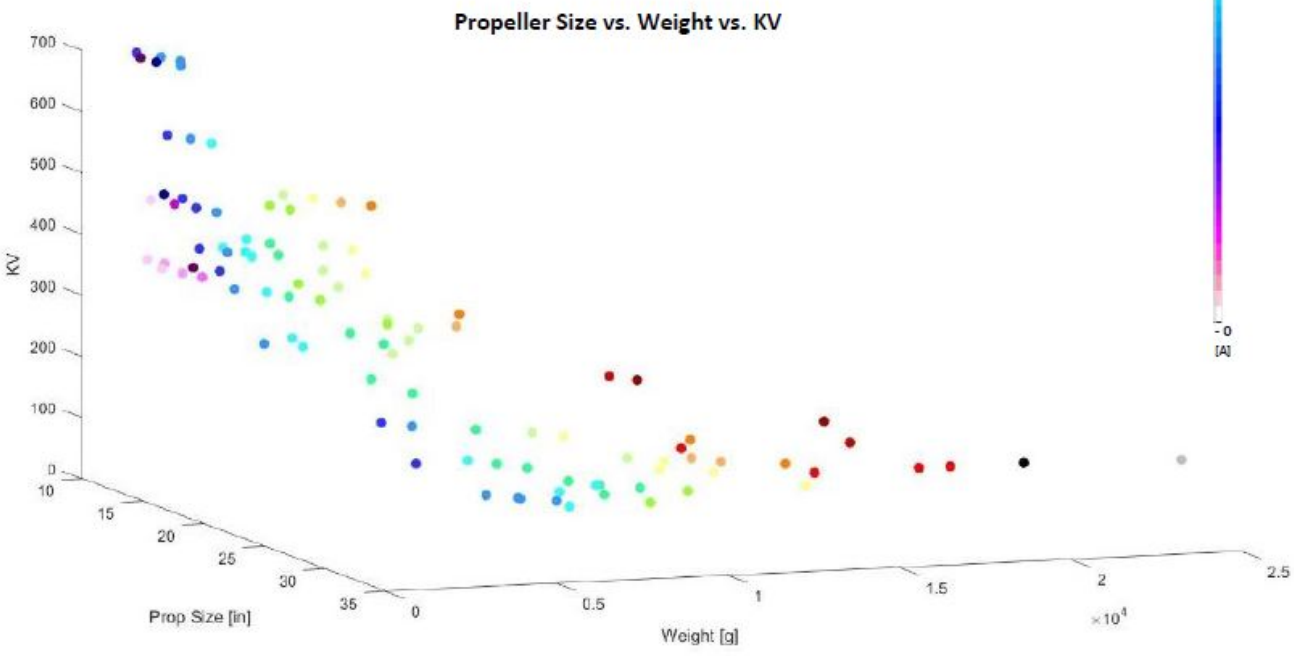

(b)

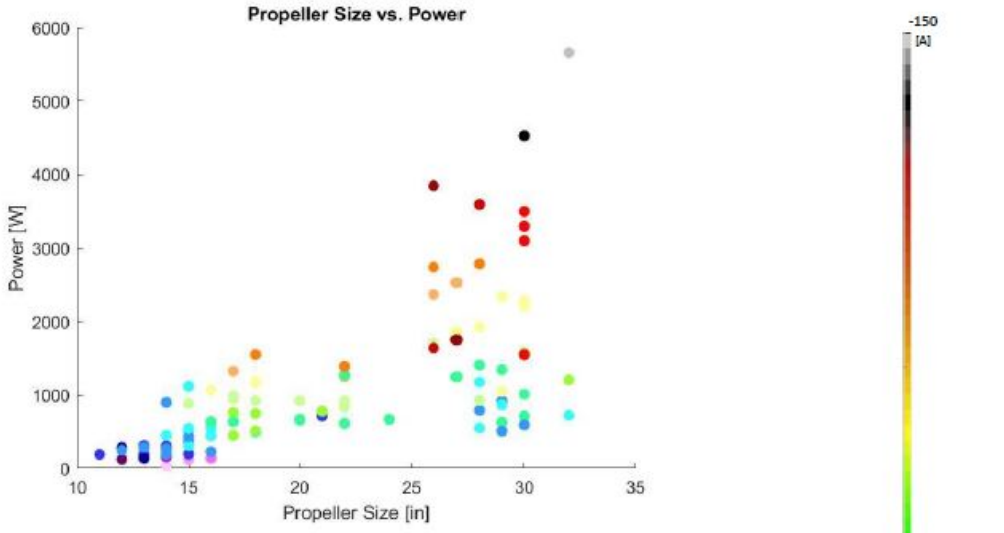
Propeller Size vs. Power
Power [W]
Propeller Size [in]
-150
[A]
0
[A]

(c)

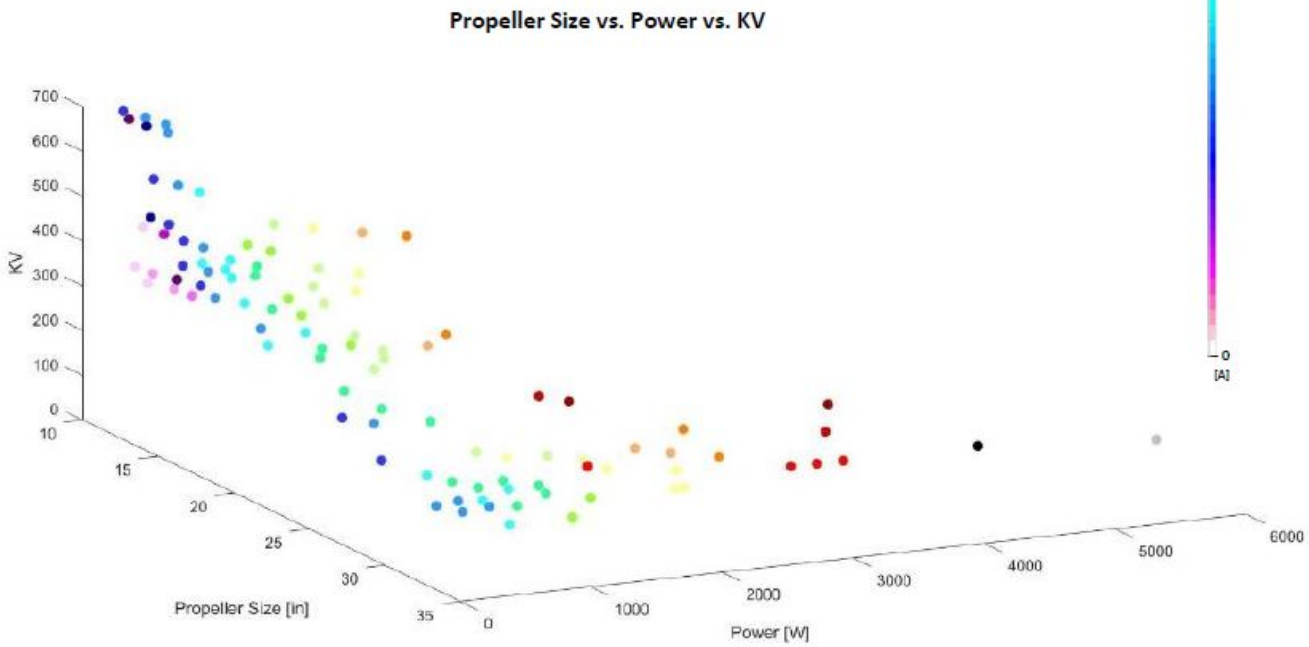
Propeller Size vs. Power vs. KV
KV
Propeller Size [in]
Power [W]

(d)

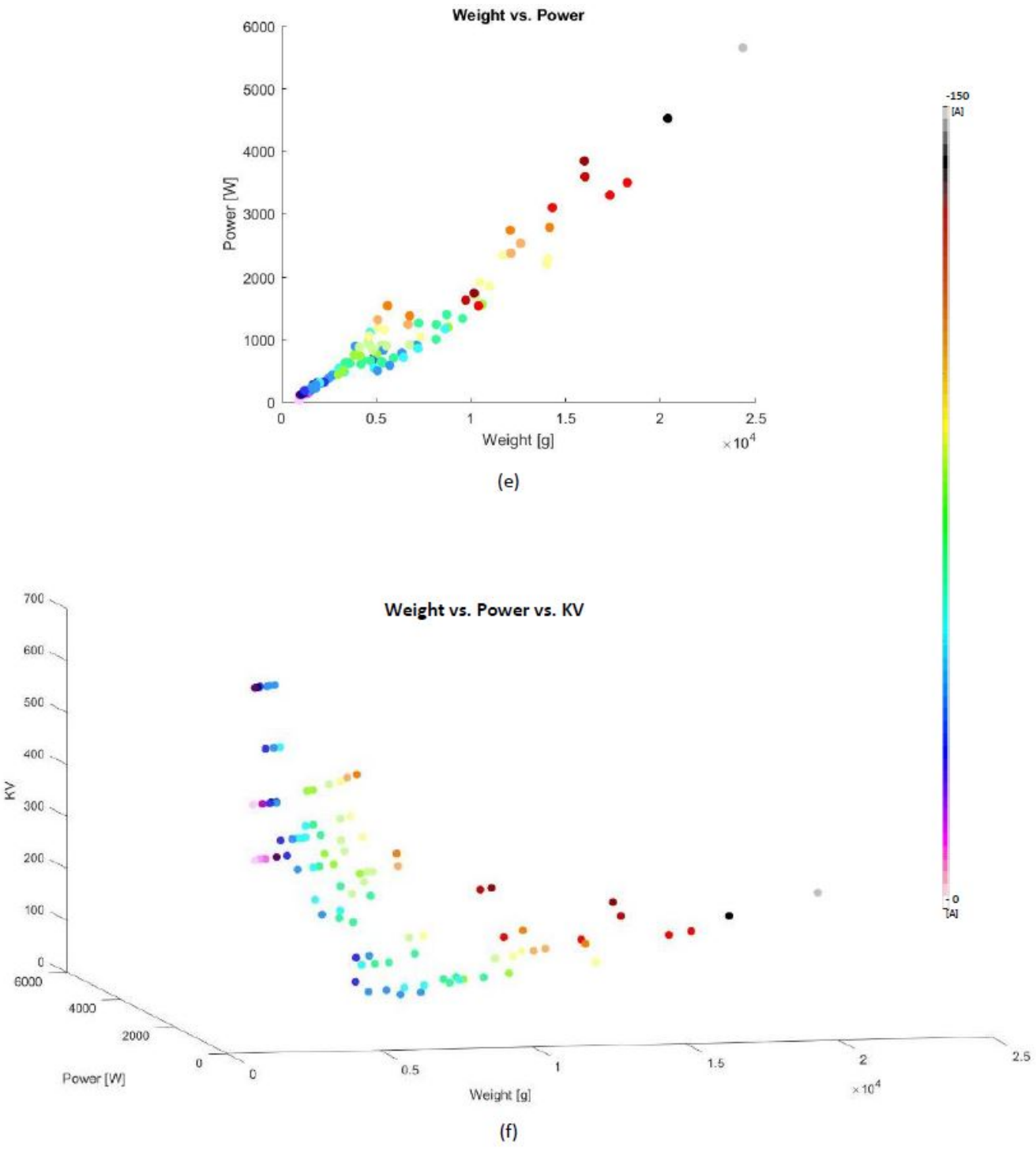

Figure 3.12: Graphical representation of Propeller Size vs. Weight (thrust) (a & b), Propeller Size vs. Power (c & d) and Weight (thrust) vs. Power (e & f). Taken from 100 datasheets of T-motor motors [58].

3.2.2 Final Attempt

The previous mentioned 100 motors coupled with the suggested components, where taken to form 100 quadcopters (multirotor with 4 motors, each with its own propeller). Each of the 100 configurations was modeled with the selected payload plus 50 different sizes of batteries providing the required voltage of

the motor. This approach allows to have a rough understanding of the type of multirotor needed for the required job.

The mass of each of the modeled multirotor configurations was obtained by summing up the mass of the motors, propellers and ESC (all obtained from the specs sheet of the manufacturer) plus the mass of the battery, frame and payload.

To identify the mass of the battery, an example of commercial batteries with 3, 4, 6 and 12 cells (1 cell = 3.7 V), was taken each with its respective mass, energy, and discharge rate. Additional battery sizes were given an estimated mass according to the linear approximation between the energy of the example batteries and their mass. Figure 3.13 displays the linear trend of the mass of LiPo batteries and their energy where the stars represent real commercial batteries.

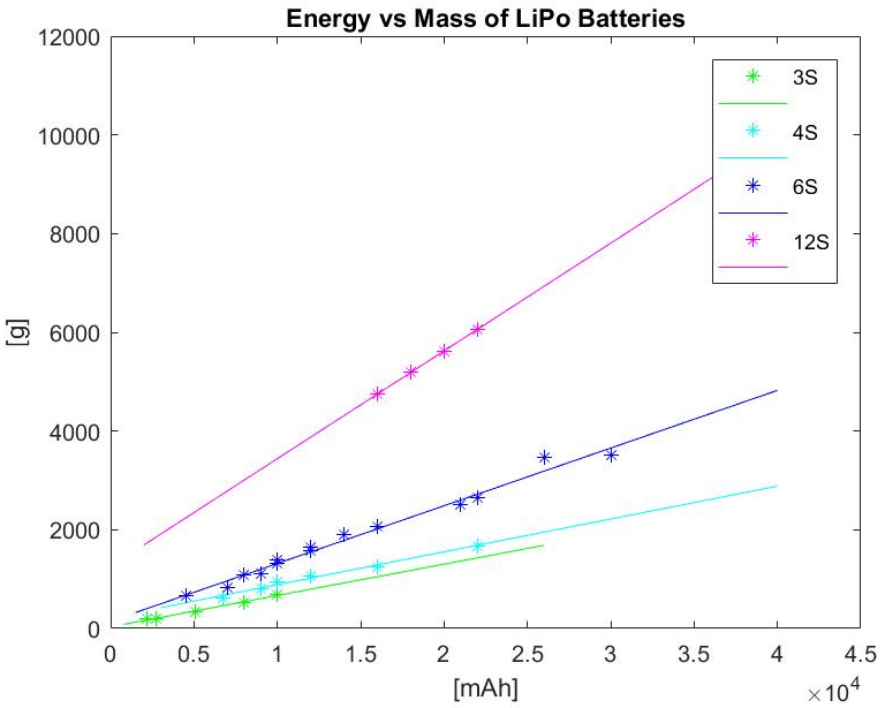

Figure 3.13: Linear regression line of commercial LiPo batteries.

The mass of the frame is an assumption defined as a function of the propeller's diameter considering that 0.045 kg is the weight of a 7 x 9 mm x 1000 carbon fiber tube [59]. Finally the mass of the payload is equal to the mass of the cleaning device plus mass of the water fitted into it.

The weight is then translated into the required thrust in [N] per motor ($T_{\text{motor}} = 9.81 \cdot m/4$).

To simplify the model, all the calculations carried from now on, assume that the multirotor is at hover.

After knowing the required thrust, it is possible to calculate the ideal theoretical power consumed by the motor using Eq. (2.7). Then, the figure of merit ($M = 0.6$) is used to approximate the real power consumed by the rotor ($P = P_{\text{ideal}}/M$).

To find the flight time of the specific multirotor it is necessary to account the battery specifications such as voltage (V) and energy (mAh). The current consumed by the motor is $I_{\text{motor}} = P/V_{\text{battery}}$. To estimate the total current withdrawn from the battery it is assumed that the ESC and other components

consume 10% of the total current while the motors consume the rest 90% [60]. Therefore, total current withdrawn from the battery can be calculated by $I_{\text{battery}} = (4 \cdot I_{\text{motor}})/0.9$.

Before modeling all the multirotor configurations with the decided payload, the configurations that do not practically comply with the weight requirements are eliminated with 2 conditions:

1. The maximum thrust that the propeller can achieve has to be greater than 2 times the weight of the multirotor [61]

2. The maximum current given by the battery must be greater than 1.5 times the withdrawn current from motor as a conservative assumption decided by the researcher to avoid motor failures.

The flight-time of the complying configurations is then calculated ($t_{\text{flight}} = E_{\text{battery}}/I_{\text{battery}}$). The configuration with the longest average flight-time, obtained with all battery sizes, is selected as the reference configuration which states a motor type, a propeller size, an ESC, an input voltage and a total weight. The user can also visualize the results and manually select the preferred configuration according to the specific needs.

A larger propeller achieves longer flight-times because it needs to spin slower to generate the same lift and thrust causing the induced velocity to decrease. Thereby, From Eq. (2.7) the power losses decrease as well.

Other reason why an operating multirotor with larger propellers result in longer flight-times is because once the propeller is spinning, the rotational inertia facilitates to maintain the rotational speed. At the same rotational speed, a bigger rotor area provides more thrust than a smaller rotor area, therefore, the required power to produce a certain thrust is less for a bigger propeller. Less power needed means less withdrawn current from the battery which results in a longer duration of the battery and consequently, a longer flight-time. At the same time, the rotational inertia, $\mathcal{I}$, that maintains the propeller spinning limits the maneuverability of the multirotor since a rotating propeller with higher inertia is more difficult to slow down or stop. The rotational inertia explains the torque of a rotor according to 2$^{\text{nd}}$ Newton's Law for rotational motion $Q = \mathcal{I}\ddot{\alpha}$, where $\ddot{\alpha}$ is the angular acceleration. As mentioned in section 2.2, the multirotors are maneuvered by accelerating or decelerating the rotation of the propellers, therefore, the torque produced by the rotor is a reference for the multirotor's maneuverability.

It is important to identify the flight purposes and conditions to understand the torque limitations for maneuverability. Furthermore, the motor's limit on how much current it can handle to produce a certain torque, must be considered so that the selected propeller does not over heat the motor.

To evaluate the performance of the reference configuration with different propellers, a range of propeller sizes is selected around the reference propeller size. According to the shape of each propeller (diameter, pitch and assumed cord). The manufacturer specifies the propeller's diameter and pitch angle but does not specify the section cord or the superficial area. The area of the propeller was calculated by assuming that each blade is an oval whose minor radius depends on the given major radius. This assumption allows to define the solidity ratio as $\sigma = N \cdot A_{\text{blade}}/A_{\text{disk}}$.

By just knowing the shape of the propellers blades, specifically, the solidity ratio and the pitch angle, it is possible to use Eq. (2.28) to calculate the inflow ratio. The inflow ration is then used to find the

thrust coefficient, power coefficient and torque coefficient with Eq. (2.24) and (2.26).

The required thrust is obtained with the weight of the multirotor. Having the required thrust, Eq. 2.20, 2.21 and 2.22 are used with the previous obtained obtained C_T, C_Q and C_P to obtain the RPM, power and torque.

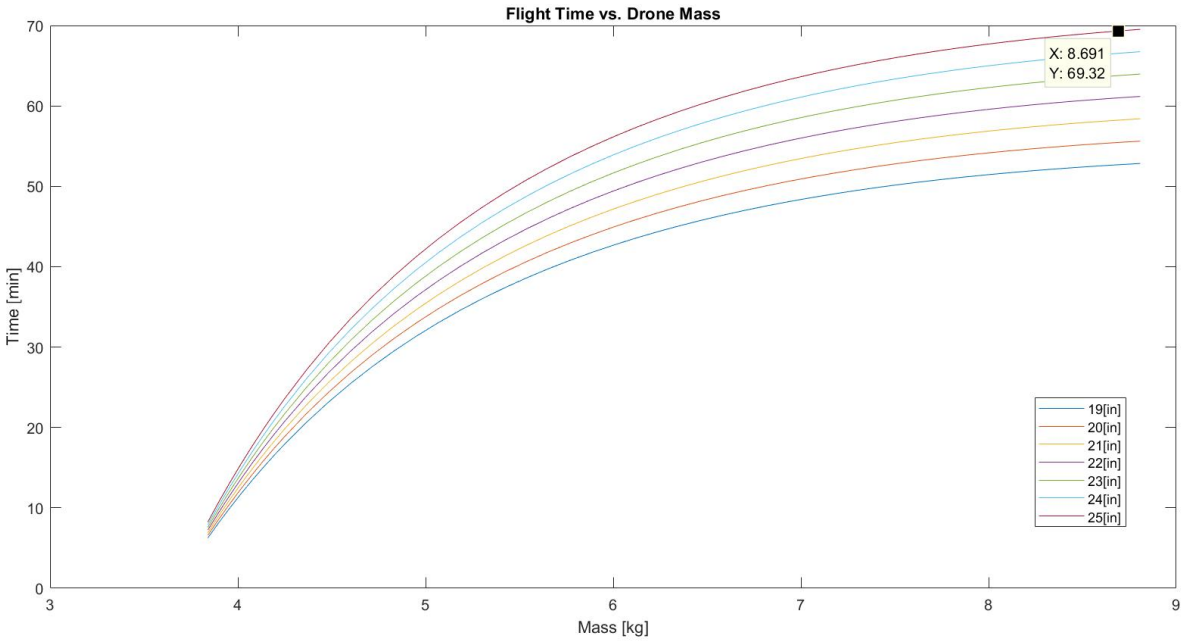

Figure 3.14: 2.5 kg multirotor modeled with 6S batteries ranging from 1500 mAh to 44 000 mAh with propeller sizes ranging from 19 in to 25 in and 1 kg payload.

The total mass of the multirotor with each of the batteries is used to graph mass vs. flight-time for each different propeller. For example, figure 3.14 shows the resulting graph for a 2.5 kg multirotor plus 1 kg payload and different battery sizes. The last value pointed in the graph corresponds to the highest theoretical flight-time (for the range of chosen batteries) for a multirotor at hover with a propeller size of 25 in.

The first section of Figure 3.14 has the highest increase in flight-time for an additional unit of battery size. As the batteries get heavier the graph starts to flatten down, meaning that the addition of battery capacity turns inefficient. Therefore, the multirotor design configuration was taken from shorter flight-times before the curve starts to flatten down to attain the best performance of the multirotor in respect to the battery size.

Finally, different flight-times are selected below the highest theoretical flight-time to see the performance of the reference multirotor with each propeller for every chosen flight-time in terms of continuous RPM, Power withdrawn from battery, Torque as well as battery size and weight.

3.3 Model Validation

To validate the model, six aleatory motors with their suggested propellers where chosen from the data-sheets of T-Motor and plotted, as red crosses, on top to the blue line graphs generated by the model that simulates, thrust, power, torque and flight-time given the RPM and propeller specifications. The results are displayed in the figures below.

The thrust and power of the samples closely follow the model's graphs. In the other hand, the modeled torque slightly deviates from the data-sheet points. This is due to the assumption explain in section 2.4.2 where the torque is obtained with the torque coefficient, C_q that is assumed to be equal to the power coefficient, C_p.

The flight-time for smaller propellers is also closely estimated whereas for bigger propellers the model gives slightly higher flight-times since the model only considers hover while the flight-time specification of the manufacturer also considers take-off and maneuverability which requires higher power for bigger propellers.

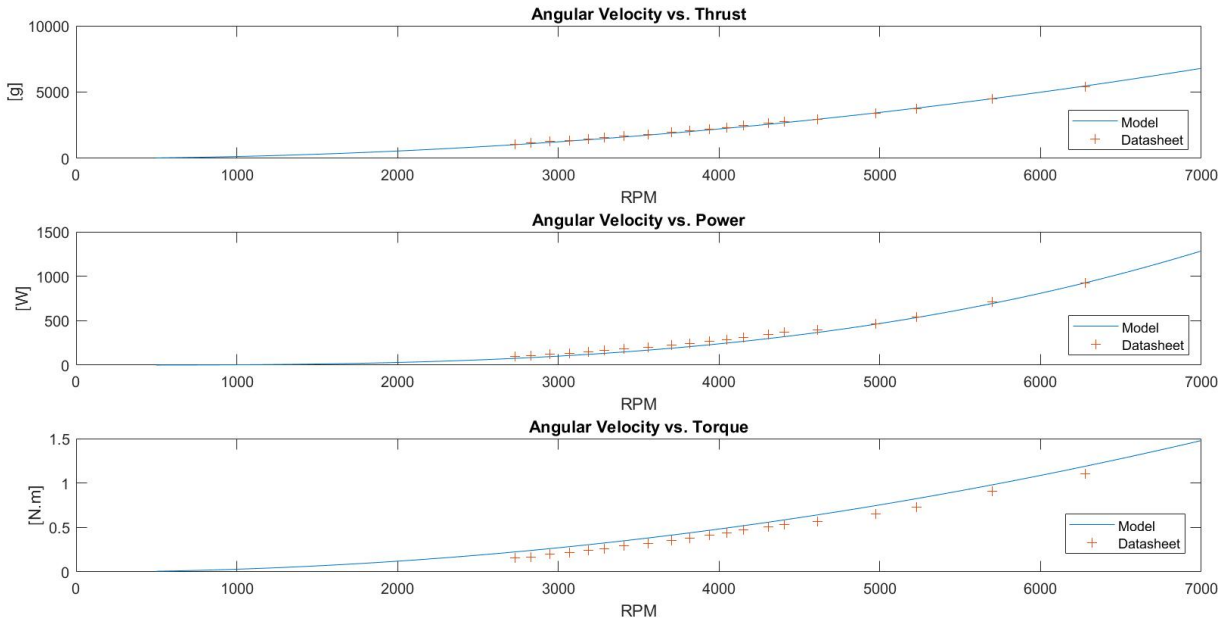

Figure 3.15: Thrust, Power and Torque of motor MN505 K_v320 with propeller 20 in$\times$6 in found at: T-Motor [58]

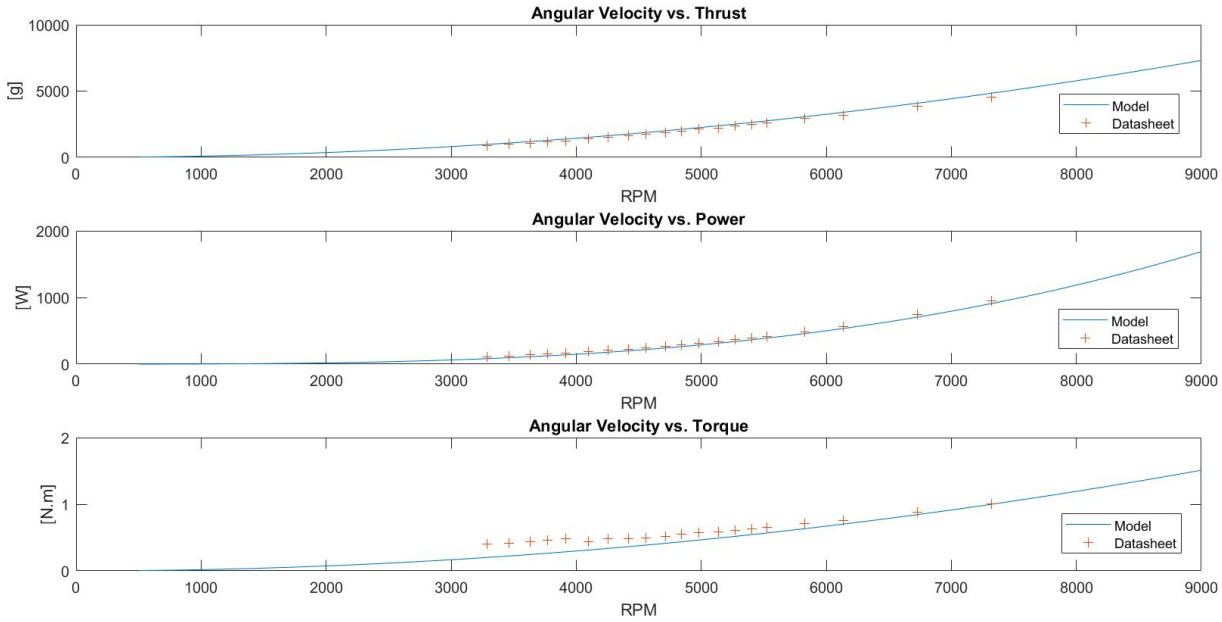

Figure 3.16: Thrust, Power and Torque of motor MN505 K_v320 with propeller $17\,\text{in} \times 5.8\,\text{in}$ found at: T-Motor [58]

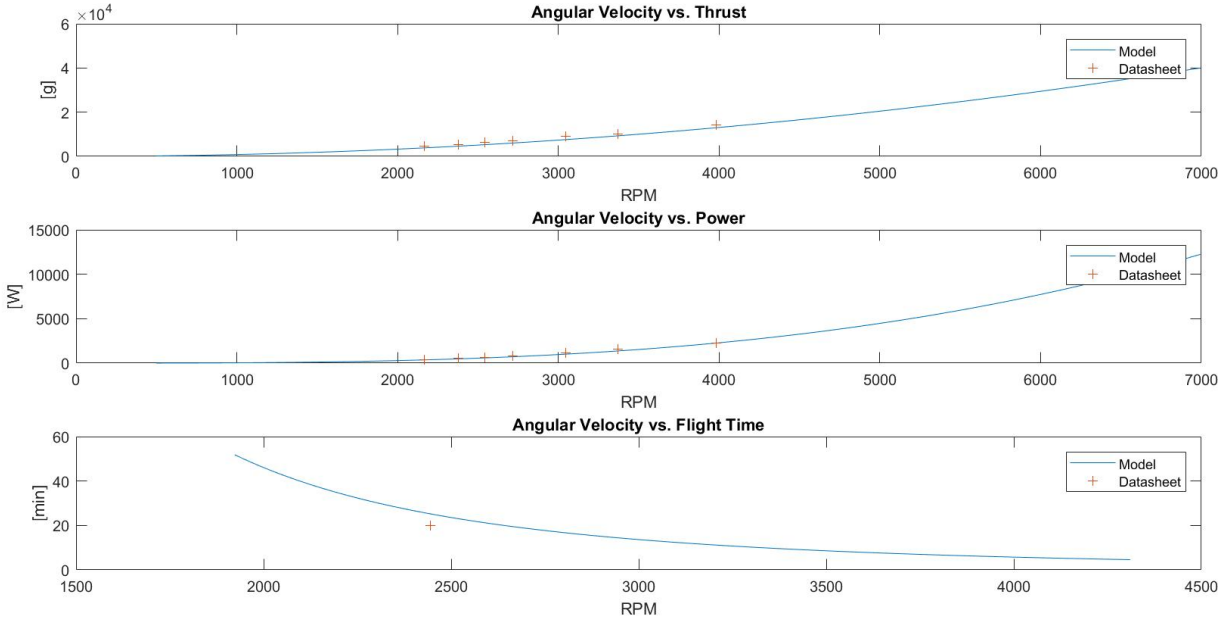

Figure 3.17: Thrust, Power and Flight-time of motor P80 K_v100 with propeller $30\,\text{in} \times 10.5\,\text{in}$ found at: T-Motor [58]

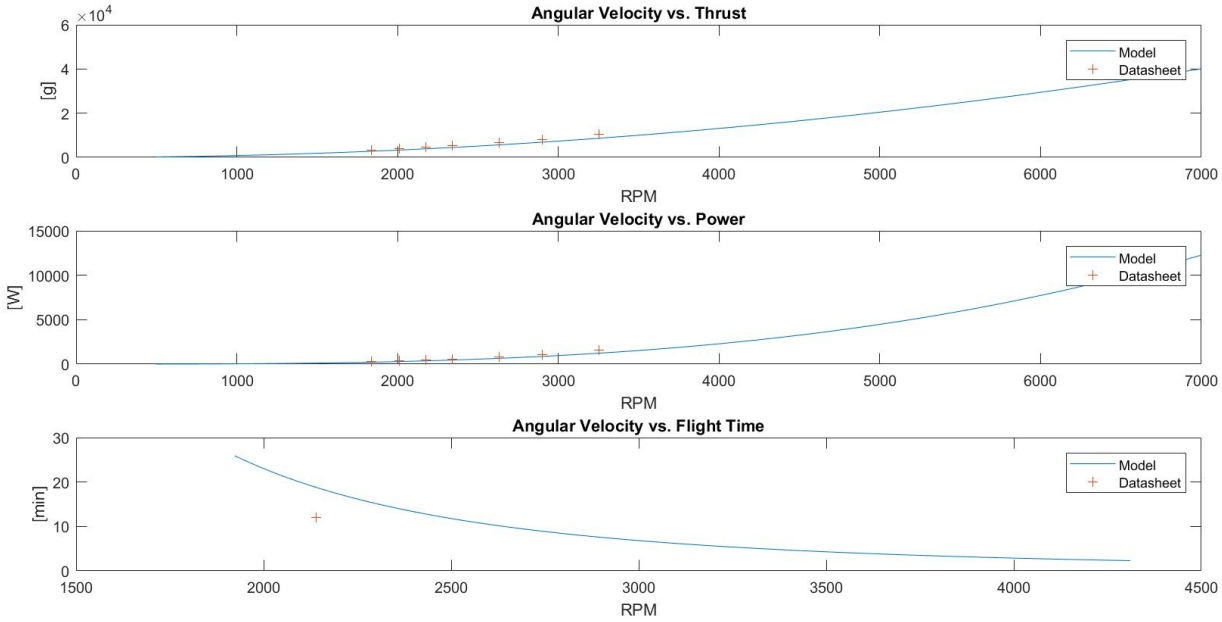

Figure 3.18: Thrust, Power and Flight-time of motor P80 K_v170 with propeller $30\,\text{in}\times10.5\,\text{in}$ found at: T-Motor [58]

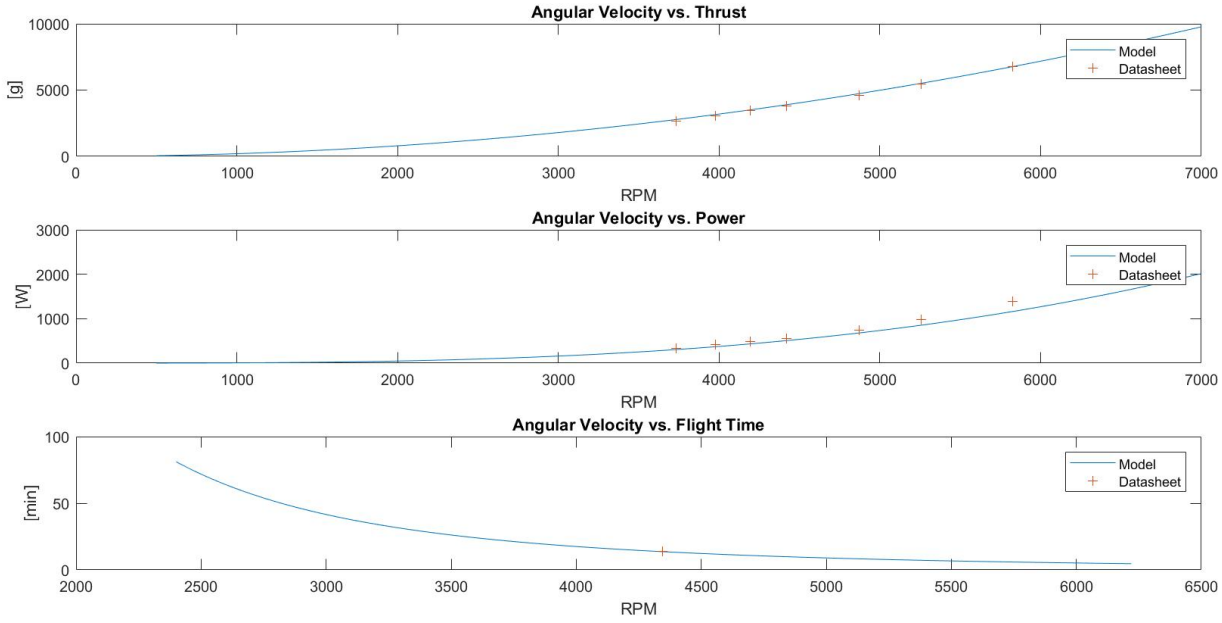

Figure 3.19: Thrust, Power and Flight-time of motor P60 K_v340 with propeller $22\,\text{in}\times6.6\,\text{in}$ found at: T-Motor [58]

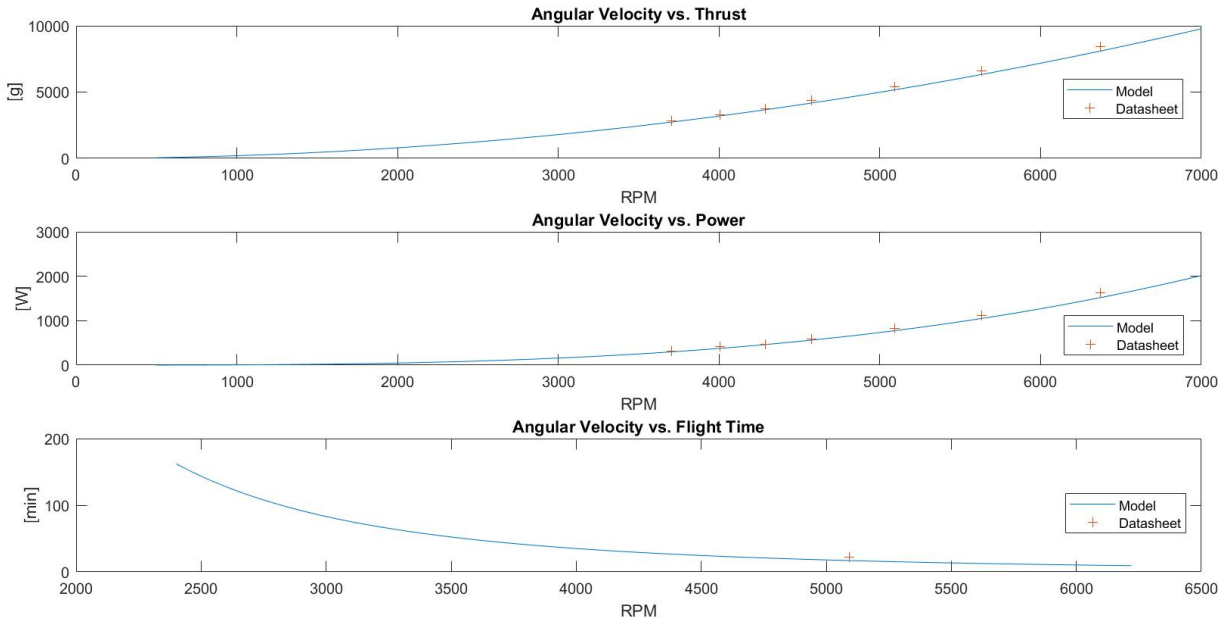

Figure 3.20: Thrust, Power and Flight-time of motor P60 K_v170 with propeller $22\,\text{in} \times 6.6\,\text{in}$ found at: T-Motor [58]

Chapter 4

Results and Discussion

4.1 Flight-Path Model

The selected path was with four devices per multirotor in ”zig-zag” sketch for both, Base Station scenario and Cart scenario (Figure 3.8 and Figure 3.10). 4 cleaning devices maintain the multirotor as occupied as possible since 5 devices would result in 30 s of waiting time, which does not comply with the 1 min buffer constrain. The resultant outputs, to clean the entire field with the selected path for the Central Station scenario, with the first assumption (1 L of water is fitted into each device at a time) are displayed in Table 4.1.

Table 4.1: Results for multirotor's path on Central Station scenario with 4 cleaning devices carrying 1 L of water each.

Total water per device	9.04 L
Total airborne time	7 h 40 min
Idle time per set of mirrors	1 min 23 s
Total time to clean field	10 h 46 min

The purpose of the path modeling is to state an idea for the required payload of the multirotor, which directly depends on the amount of water fitted into each device. The multirotor will fly longer as the payload is lighter, so it is required to identify the optimal minimum amount of water to fill into the device at a time.

The Cart scenario has the availability to refill the water at any point in the cleaning process, therefore, the water refilling in the Cart scenario is independent of the multirotor's battery recharging. To understand advantages of reducing the weight of the payload/water to be carried versus the extra flight time to recharge the cleaning devices more often, two settings were modeled. (1) 1 L of water is fitted into the cleaning device (2) 0.5 L are of water are fitted into the cleaning device. The comparison of the two settings for the time to clean field and gained flight-time is shown in Table 4.2 and Figure 4.1 respectively.

The total airborne time increases by 11 min and the flight-time for each cleaning cycle can increase form 7-12 min, therefore it is favorable to decrease the quantity of water. 4 devices each with 0.5 L can clean 28 heliostats per refiling cycle, assuming this as a reasonable amount, the decided amount of water to be fitted into the devices of the Cart scenario is 0.5 L of water.

Table 4.2: Results for multirotor's path on Cart scenario with 4 cleaning devices carrying (a) 1 L of water each (b) 0.5 L of water each.

(a)

Total airborne time	7 h 7 min
Idle time per set of mirrors	1 min 23 s
Total time to clean field	10 h 13 min

(b)

Total airborne time	7 h 17 min
Idle time per set of mirrors	1 min 23 s
Total time to clean field	10 h 23 min

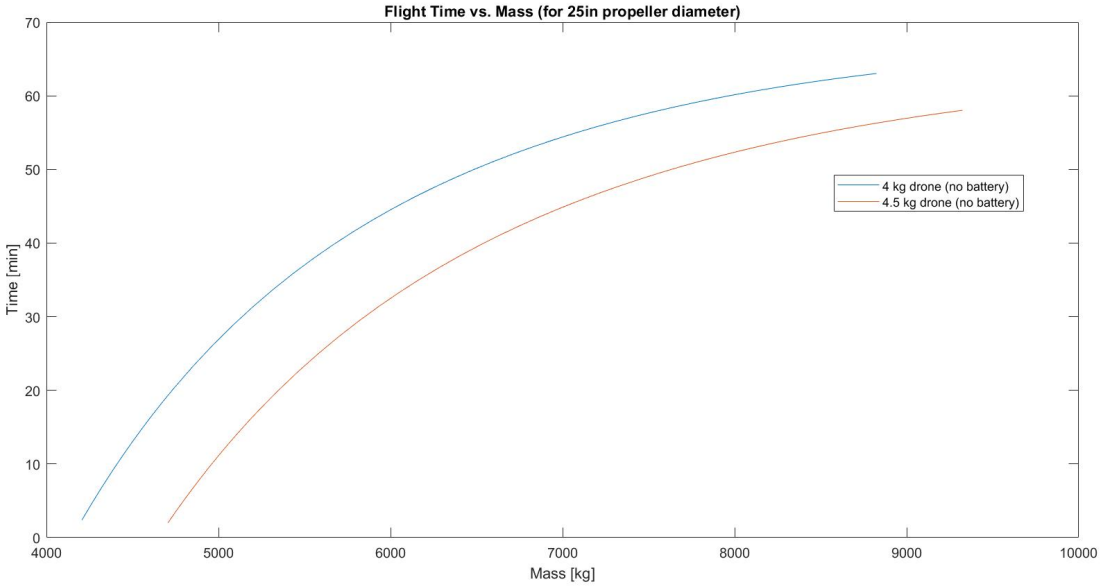

Figure 4.1: Mass of multirotor plus battery vs. flight-time of 4 kg and 4.5 kg quadrotor.

For the Central Station scenario, it is necessary to understand the operational requirements of the field in terms of how often the mirrors need to be cleaned. As the field is an imaginary example field, there are not specific operation requirements, so the most common cleaning requirements are taken as a reference. Generally, the heliostats in the CSP plants located in the Northern Cape of South Africa are expected to be cleaned every 7 days[1]. Dividing the entire field's cleaning job into 7 days would mean that each day 78 heliostats need to be cleaned and 1.3 L of water would be used per cleaning device per day. If the total time required to clean the field divided by how often the mirrors should be cleaned is more than 24 hours it is required to add an additional multirotor. An additional multirotor would reduce the total cleaning time to half. For the example case, 1 multirotor is enough to compile with the cleaning requirements.

1.3 L of water per device, per day, will clean the entire heliostat field in 7 days. The entire job must be divided into days because large CSP plants have hundreds of thousands of m^2 of mirrors [62] and diving the cleaning work into days is a most. Furthermore, it would be ideal to use the night hours to perform the cleaning work in order not to interfere with the thermal performance of the field.

To optimize the flight-path of the multirotor, the water refilling is matched with the recharging of the multirotor's battery. At this point, the flight-time of the multirotor is unknown. Once the flight-time is known the airborne time per day is divided into the flight-time to obtain the recharge times per day which

[1] This information was given to the researcher at the technical visit of the CSP plants.

equal the cleaning cycles per day. The 1.3 L of water will then be divided into the cleaning cycles to obtain the amount of water fitted into the device.

4.2 Drone Sizing Model

With the first assumption of water fitted into the device, the payload is equal to 1 kg of water plus 2 kg of the cleaning device itself. A payload of 3 kg is inserted into the model, and the resulting reference configuration is displayed in Table 4.3.

Table 4.3: Results for the reference multirotor components.

Configuration N°	94
Motor	120K_v/ 772 g / Peak Current 57.3 A / Max Power 2783 W
Propeller	27 in × 8.8 in/ 92 g/1900 rpm-4300 rpm
Battery voltage	12S (44.4 V)
ESC	Flame 80 A
Theoretical Flight-Time	51 min
Drone weight (NO battery, NO payload)	5863 g

The combination of the reference motor with the reference ESC is modeled with 7 propellers sizes (reference propeller ± 3 in) and 50 different 12S battery sizes from 2000 mAh to 50 000 mAh. The resulting behavior is provided in the Figure 4.2.

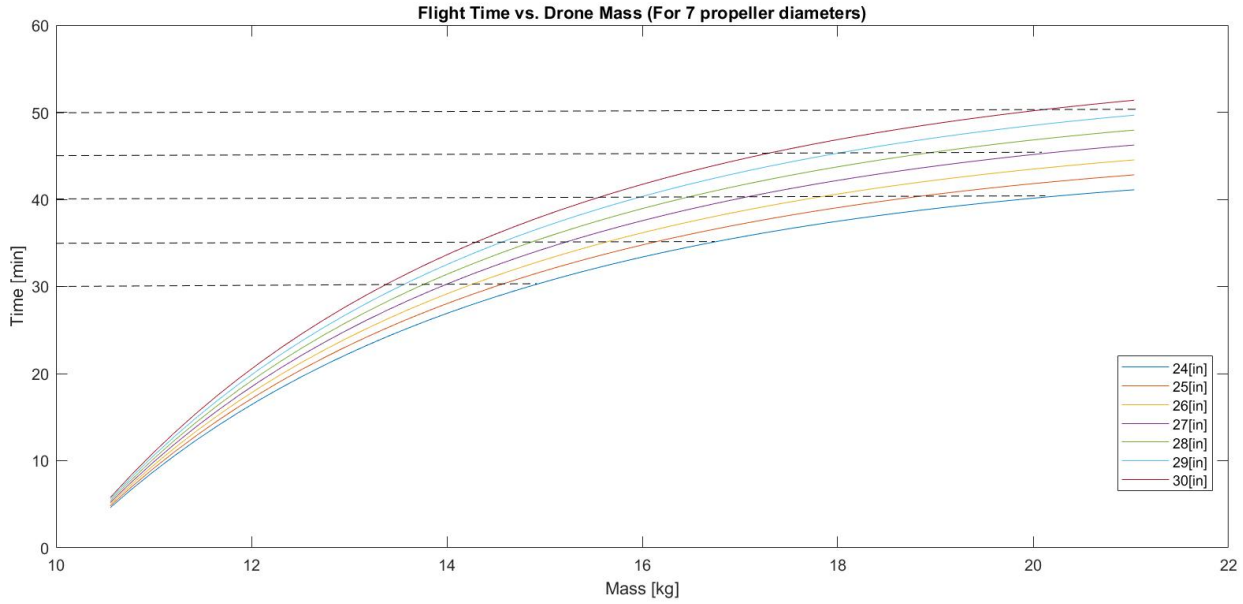

Figure 4.2: Flight-time for a 8.6 kg quadrotor (including payload) with batteries from 2000 mAh to 50 000 mAh and 7 propeller sizes.

Table 4.4: Diameter and pitch of the propellers plus the battery energy to attain the indicated flight-time for the all up weight (AUW) of a hovering quadcopter. RPM, power and torque, to attain the required thrust at hover, is indicated for each propeller.

Flight-Time: 30 min

Diameter_in	pitch_in	Batt_Energy_mAh	Batt_Weight_g	AUW_g	RPM	Power_W	Current_A	Torque_Nm
24	7.7	22000	6059	14922	3623	436	9	0.97
25	8.1	20000	5623	14486	3267	400	8	0.99
26	8.4	19000	5404	14267	3004	376	8	1.01
27	8.7	18000	5186	14049	2769	354	7	1.03
28	9	17000	4968	13831	2560	333	7	1.05
29	9.4	16000	4750	13613	2353	314	7	1.08
30	9.7	15000	4531	13394	2185	296	6	1.09

Flight-Time: 35 min

Diameter_in	pitch_in	Batt_Energy_mAh	Batt_Weight_g	AUW_g	RPM	Power_W	Torque_Nm
24	7.7	30000	7806	16669	3830	514	1.08
25	8.1	28000	7369	16232	3459	475	1.11
26	8.4	25000	6714	15577	3139	429	1.1
27	8.7	23000	6278	15141	2875	396	1.11
28	9	22000	6059	14922	2659	373	1.13
29	9.4	20000	5623	14486	2427	345	1.14
30	9.7	19000	5404	14267	2255	326	1.16

Flight-Time: 40 min

Diameter_in	pitch_in	Batt_Energy_mAh	Batt_Weight_g	AUW_g	RPM	Power_W	Torque_Nm
24	7.7	45000	11080	19943	4189	673	1.29
25	8.1	39000	9770	18633	3706	584	1.27
26	8.4	35000	8897	17760	3352	522	1.25
27	8.7	32000	8242	17105	3056	475	1.25
28	9	29000	7587	16450	2791	432	1.25
29	9.4	27000	7151	16014	2552	401	1.27
30	9.7	25000	6714	15577	2356	372	1.27

Flight-Time: 45 min

Diameter_in	pitch_in	Batt_Energy_mAh	Batt_Weight_g	AUW_g	RPM	Power_W	Torque_Nm
27	8.7	45000	11080	19943	3300	598	1.46
28	9	40000	9989	18852	2988	530	1.43
29	9.4	36000	9116	17979	2704	477	1.42
30	9.7	33000	8461	17324	2485	436	1.41

Flight-Time: 50 min

Diameter_in	pitch_in	Batt_Energy_mAh	Batt_Weight_g	AUW_g	RPM	Power_W	Torque_Nm
29	9.4	50000	12172	21035	2925	603	1.66
30	9.7	45000	11080	19943	2666	539	1.63

The graph rectifies that the bigger the propeller, the longer resulting flight-time. As mentioned previously, bigger propeller is not always better because of the increase in torque which limits the fast response of the multirotor and therefore compromises the maneuverability. In addition, the current needed to start, stop or slow down the propeller can overheat the motor by exceeding its peak current.

The highest theoretical flight-time achieved with the range of batteries is 51 min and states the reference from which lower flight-times are chosen to evaluate the correspondent multirotor configuration, each with a range of propellers. 50, 45, 40, 35, and 30 min of flight-time is inserted into the model to obtain the results in Table 4.4.

The next step is to obtain the power needed to take-off and stop the propellers of each multirotor combinations in Table 4.4 to see if it is over or under the peak current of the motor. Only the combinations within a safety margin under the peak current are selected and the one with longest flight-time will be chosen as multirotor configuration.

In the example case, the power to take-off or stop the propellers was not calculated. Figure 4.1 shows that if the workload is divided into 7 days, the required flight time per day is 1 h 6 min. A 1 h flight-time multirotor is hardly achieved and, from the longest reference flight-time of 51 min, it was understood that the multirotor's battery should be recharged at least one time per day, which corresponds to a flight-time of 33 min. It was decided by the researcher to add a 7 min margin of extra time to account for the additional power required to take-off. As a consequence, the design flight-time is decided to be 40 min. Given this assumption, 2 cleaning cycles have to be done per day.

It is now possible to identify the amount of water fitting into each cleaning device per cleaning cycle at the Central Station scenario. Dividing the total water required to clean the field by 7 days, by 2 cycles per day, by 4 cleaning devices results in 0.65 L of water in each cleaning device per cycle. It was decided by the researcher to add 0.15 L of safety margin of water in case of any leakage. As a consequence, the decided water to fit in each device per cleaning cycle is 0.80 L. The initial assumption of 1 L is readjusted to 0.8 L and the battery charging time of 1 h is added to the Path Model. Results are displayed in Table 4.5.

Table 4.5: Results for multirotor's path in Central Station scenario with 4 cleaning devices carrying 0.8 L of water each.

Total airborne time	7 h 52 min
Idle time per set of mirrors	1 min 23 s
Total time to clean field	17 h 58 min

The total airborne time slightly increased since the water has to be refilled more often. In the other hand, the total time to clean the field significantly increased after 1 hour a day was added to charge the battery. 17.96 h of cleaning are easily achieved in 7 days and therefore, nothing is further iterated for this constrain.

In the Cart scenario the multirotor should also recharge the battery at least one time per day given that it has 1 h and 3 min of airbore time a day. Table 4.6 shows the final results for the Cart scenario after adding the total of 7 h of battery charging time and extra flight-time to recharging station.

For the selected example field, the cart only reduces by 3% the time to clean the entire field. Con-

Table 4.6: Results for multirotor's path in Cart scenario with 4 cleaning devices carrying 0.5 L of water each.

Total airborne time	7 h 18 min
Idle time per set of mirrors	1 min 23 s
Total time to clean field	17 h 24 min

sidering that the cart requires significant costs, it was decided that, for a heliostat field with the example size, the advantages of the cart are not enough to justify its costs. In the other hand, on a significant larger heliostat field, the distances to refill the water will be significantly bigger, thus a cart or specific recharging station within the field could reduce more significantly the flight-time of the multicopter.

For the chosen motor, the manufacturer suggests 26, 27 or 28 in propellers. For the purposes of the multirotor and the relative low payload, it is reasonable to consider bigger propeller sizes than the suggested ones, to achieve longer flight-times. However, their suitability should be verified as mentioned before with the detailed technical specifications of the motor or experimentally. Since the technical limitations of the motor were not measured in this research, the manufacturer suggestions are considered for a safe choice and the 28 in propeller is chosen because it achieves the decided flight-time 40 min with smaller battery than the 27 in propeller and a smaller torque than the 29 in propeller which results in less weight and more operation flexibility. Table 4.7 highlights in the yellow square the different multirotor configurations for the assigned flight-time of 40 min and payload.

Table 4.7: Specification of 7 multirotor configurations designed for 40 min flight-time and 2.8 kg payload.

Flight-Time: 40 min

Diameter_in	pitch_in	Batt_Energy_mAh	Batt_Weight_g	AUW_g	RPM	Power_W	Torque_Nm
24	7.7	45000	11080	19943	4189	673	1.29
25	8.1	39000	9770	18633	3706	584	1.27
26	8.4	35000	8897	17760	3352	522	1.25
27	8.7	32000	8242	17105	3056	475	1.25
28	9	29000	7587	16450	2791	432	1.25
29	9.4	27000	7151	16014	2552	401	1.27
30	9.7	25000	6714	15577	2356	372	1.27

Table 4.8: Component summary for the chosen multirotor configuration with a 40 min flight-time

Motor	120K_v/ 772 g / Peak Current 57.3 A / Max Power 2783 W
Propeller	28 in × 9.2 in/ 98 g/ 1500-3700 rpm
Battery	12S (44.4 V)/ 29 000 mAh
ESC	Flame 80 A/ 109 g
Thrust (55% - 65% throttle)	30 000 g
Multirotor weight (NO payload)	13 250 g
Payload	2800 g
Flight-Time	40 min
Price	≈ 3100 USD

Table 4.8 shows the specifications of the components for the final chosen multirotor. Motor, propeller and ESC are taken from the manufacturer, T-Motor [58]. It is important to note that the thrust generated by the 4 propellers at around 60% throttle (which is the manufacturers reference throttle), closely follows

the previous explained rule of thumb that states that the thrust generated by the multirotor should be at least twice the weight of itself. In this case, the thrust is $30\,\mathrm{kg}$ and the total/all up weight (AUW) is $16.5\,\mathrm{kg}$. A rough estimation was added for the price of the final chosen multirotor. The biggest driving cost are the motors each at a price of 350 USD. The cost of the propellers is 622 USD and the cost of a battery of the needed size is around 800 USD. The rest of the costs goes for the ESC, flight-control, cables and frame.

Chapter 5

Conclusions

The developed model framed a strategy to identify the required characteristics of a multirotor whose purpose is to transport one or several cleaning devices through a CSP heliostat field. It is concluded that the model is a suitable high-level estimation for choosing a multirotor with the above mentioned purposes.

5.1 Achievements

A high-level model was developed to estimate the size and characteristics of a multirotor. The model was divided into two submodels, one that defines the flight-path of the multirotor through the field and the other one that estimates the size of the multirotor. The outputs of both submodels serve as inputs for the partner submodel resulting as a whole iterative model that readjusts the first assumed inputs to arrive into the final estimations of the multirotor size in terms of battery, propeller and motor and the path characteristics of the multirotor through the heliostat field.

The outputs of the Flight-Path model; *Total Water to Clean Field, Total Airborne Time, Multirotor Idle Time* and *Total Time to Clean Field* are used to identify the payload and Flight-time of the Multirotor Sizing model whose output; *Cleaning Cycles per Day*, is used to readjust the *Water Fitted Into the Device* and *Total Ttime to Clean Field*.

The model concludes that for a field of 540 heliostats with mirrors of $2.23\,\mathrm{m}^2$, a quadcopter should carry 4 cleaning devices in parallel. If the field holds a cart, each of the 4 cleaning devices should be refilled with $0.5\,\mathrm{L}$ of water. However, for such a heliostat field size the addition of a cart is not justified. If the multirotor needs to come back to the central station, the devices should be refilled with $0.8\,\mathrm{L}$ of water each, every cleaning cycle. In this scenario, the total time to clean the field is $17\,\mathrm{h}$ and $58\,\mathrm{m}$.

A multirotor with $28\,\mathrm{in}$ propeller size and a $29\,000\,\mathrm{mAh}$ with hover flight-time of $40\,\mathrm{min}$ will carry a $2.8\,\mathrm{kg}$ cleaning device at a time. The multirotor will do two cleaning cycles per day. It will recharge the battery before initiating the first cycles and and in between cycles.

The presented methodology gives an understanding of the requirements and implications of the necessary work required to choose a cleaning technology that involves an ultrasonic cleaning device

coupled with a multirotor. The portrayed model allows the user to test different strategies for autonomous CSP plant heliotat cleaning methodologies, while the presented results picture the opportunities and advantages of the purposed cleaning technology.

5.2 Future Work

The concluding results show that the model is able to frame a strategy for selecting a multirotor and its flying sketch.

Whereas quadcopters are mostly used for hobby or leisure, hexacopters are mostly utilized in the professional ambit because of their advantages in specific cases. The main advantage of adding rotors to an aerial vehicle is that in the event of single rotor failure, the risk of losing altitude is reduced. Another advantage of hexacopter and octocopter is their facility to increase payload capability [63]. Nevertheless, due to heavier and higher power consumption, both hexacopters and octocopters result in shorter flight-time when compared to a quadcopter and usually more expensive [39]. Given the above mentioned, future work should be done to evaluate the advantages and disadvantages of using hexacopters or octocopters for the given job.

Furthermore, the impact of airflow generated by such a big multirotor could impact the cleaning system if it complies delicated components or if the water is exposed. Therefore, in the further research, miltirotor's generated airflow should be considered to understand the impact on the cleaning system.

Moreover, the weather conditions can significantly influence the flight performance of the multirotor. For instance, wind gusts can unbalance the thrust of individual rotors, producing a moment that, if not compensated, will destabilize the milticopter, resulting in a possible crash [64]. Therefore, weather conditions depending of the site should be added as variable to the model to understand additional multirotor's constraints.

Finally, the cost is a very important parameter that incites the decision making between different drive configurations of a multirotor. As mentioned throughout the work, bigger propellers provide longer flight-times but each motor has a limitation on how big can the coupled propeller be. Therefore, for bigger propellers again bigger motors are needed which is the biggest cost component of a multirotor. Therefore, is it encourage to add the cost of the drive configurations to the model so that the user can ease the decision making by not only comparing the performances of each configuration but also the cost.

References

[1] EPA. Sources of Greenhouse Gas Emissions. *Climate Change*, pages 1–2, 2015. URL https://www.epa.gov/ghgemissions/sources-greenhouse-gas-emissionshttp://www.epa.gov/climatechange/ghgemissions/sources/transportation.html.

[2] M. Wittmann, T. Hirsch, and M. Eck. Some aspects on parabolic trough field operation with oil as a heat transfer fluid. *Proceedings of SolarPACES*, pages 15–18, 2009.

[3] M. Lubkoll. *Performance characteristics of a spiky central receiver air pre-heater (SCRAP)*. PhD thesis, Stellenbosch: Stellenbosch University, 2017.

[4] B. Kroposki, R. Margolis, and D. Ton. Harnessing the sun. *IEEE Power and Energy Magazine*, 7(3): 22–33, may 2009. ISSN 1540-7977. doi: 10.1109/MPE.2009.932305. URL http://ieeexplore.ieee.org/document/4907278/.

[5] A. A. Merrouni, A. Mezrhab, A. Ghennioui, and Z. Naimi. Measurement, comparison and monitoring of solar mirror's specular reflectivity using two different reflectometers. *Energy Procedia*, 119:433–445, 2017.

[6] S. Bouaddi, A. Fernández-García, C. Sansom, J. A. Sarasua, F. Wolfertstetter, H. Bouzekri, F. Sutter, and I. Azpitarte. A review of conventional and innovative-sustainable methods for cleaning reflectors in concentrating solar power plants. *Sustainability*, 10(11):3937, 2018.

[7] Reduction of water consumption in concentrated solar power (csp) plants. https://www.minwatercsp.eu. Accessed in June 2019.

[8] Ultrasonic technology to clean solar panels. https://www.tekniker.es/media/uploads/noticias/NP_LimpiezaUltrasonidos_EN.pdf. Accessed: 2019-09-30.

[9] N. M. Kumar, K. Sudhakar, M. Samykano, and V. Jayaseelan. On the technologies empowering drones for intelligent monitoring of solar photovoltaic power plants. *Procedia computer science*, 133:585–593, 2018.

[10] S. Gallardo-Saavedra, L. Hernández-Callejo, and O. Duque-Perez. Technological review of the instrumentation used in aerial thermographic inspection of photovoltaic plants. *Renewable and Sustainable Energy Reviews*, 93:566–579, 2018.

[11] J. Teubner, I. Kruse, H. Scheuerpflug, C. Buerhop-Lutz, J. Hauch, C. Camus, and C. J. Brabec. Comparison of drone-based ir-imaging with module resolved monitoring power data. *Energy Procedia*, 124:560–566, 2017.

[12] M. Al-Housani, Y. Bicer, and M. Koç. Experimental investigations on pv cleaning of large-scale solar power plants in desert climates: Comparison of cleaning techniques for drone retrofitting. *Energy conversion and management*, 185:800–815, 2019.

[13] The world's first fully automated uav for cleaning solar panels – aerial power introduces the worlds first cleaning drone. 2018: London, united kingdom. https://www.aerialpower.com/solarbrush/. Accessed: 2019-09-30.

[14]] cleandrone – cleandrone 2018: Barcelona, spain. http://www.cleandrone.com/cleandrone-2/. Accessed: 2019-09-30.

[15] F. Mesas-Carrascosa, D. Verdú Santano, F. Pérez Porras, J. Meroño-Larriva, and A. García-Ferrer. The development of an open hardware and software system onboard unmanned aerial vehicles to monitor concentrated solar power plants. *Sensors*, 17(6):1329, 2017.

[16] J. E. Gouws. Calibration of heliostats using a drone. 2018.

[17] S. Yoon, H. C. Lee, and T. H. Pulliam. Computational analysis of multi-rotor flows. In *54th AIAA Aerospace Sciences Meeting*, page 0812, 2016.

[18] G. E. Cohen, D. W. Kearney, and G. J. Kolb. Final report on the operation and maintenance improvement program for concentrating solar power plants. Technical report, 1999. URL https://p2infohouse.org/ref/17/16933/1693301.pdf.

[19] S. Bouaddi, A. Fernández-García, C. Sansom, J. Sarasua, F. Wolfertstetter, H. Bouzekri, F. Sutter, and I. Azpitarte. A Review of Conventional and Innovative- Sustainable Methods for Cleaning Reflectors in Concentrating Solar Power Plants. *Sustainability*, 10(11):3937, oct 2018. ISSN 2071-1050. doi: 10.3390/su10113937. URL http://www.mdpi.com/2071-1050/10/11/3937.

[20] A. Pfahl, J. Coventry, M. Röger, F. Wolfertstetter, J. F. Vásquez-Arango, F. Gross, M. Arjomandi, P. Schwarzbözl, M. Geiger, and P. Liedke. Progress in heliostat development. *Solar Energy*, 152: 3–37, 2017.

[21] Helio100. https://helio100.sun.ac.za/. Accessed: 2019-09-30.

[22] I. D. Corporation and K. S. One. Baring the secrets of Khi Solar One — CSP Today. pages 1–2, 2013. URL http://analysis.newenergyupdate.com/csp-today/markets/baring-secrets-khi-solar-one?sthash.x5xJEr1y.mjjohttp://social.csptoday.com/markets/baring-secrets-khi-solar-one?utm{_}source=http://uk.csptoday.com/fc{_}csp{_}pvlz/{&}utm{_}medium=email{&}utm{_}campaign=CSP+Ebrief+16-09-2013+en{&}utm{_}term=Baring+the+secrets+of+Khi+Solar+One{&}utm{_}content=55374.

[23] X. Zhang, X. Liu, and Z. Wang. Research of the Heliostat Cleaning Method. In *Proceedings of ISES World Congress 2007 (Vol. I – Vol. V)*, pages 1782–1784. Springer Berlin Heidelberg, Berlin, Heidelberg, 2008. doi: 10.1007/978-3-540-75997-3_364. URL http://link.springer.com/10.1007/978-3-540-75997-3{_}364.

[24] R. S. Berg. Heliostat dust buildup and cleaning studies. *Sandia Labs., Albuquerque, NM (USA).*, (SAND-78-0432C):1–34, mar 1978. doi: 10.2172/6867834. URL http://www.osti.gov/servlets/purl/6867834/.

[25] T. S.-C. Fields. leaning Strategies for Parabolic Trough Solar-Collector Fields; Guidelines for Decisions. *Sandia National Laboratories*, jun 1981. doi: 10.2172/6376410. URL http://www.osti.gov/servlets/purl/6376410-6p7Kc0/.

[26] F. Anglani, J. Barry, and W. Dekkers. Development and Validation of a Stationary Water-Spray Cleaning System for Concentrated Solar Thermal (CST) Reflectors. *Solar Energy*, 155:574–583, oct 2017. ISSN 0038-092X. doi: 10.1016/J.SOLENER.2017.06.013. URL https://www.sciencedirect.com/science/article/abs/pii/S0038092X17305157.

[27] Ecilimp termosolar. http://www.ecilimp.com/termosolar.php. Accessed in June 2019.

[28] M. Hardt, D. Martínez, A. González, C. Garrido, S. Aladren, J. Villa, and J. Saenz. Hector – heliostat cleaning team-oriented robot. 11 2011.

[29] M. Hardt, D. Martínez, A. González, C. Garrido, S. Aladren, J. R. Villa, and J. Saenz. HECTOR – heliostat cleaning team-oriented robot. *SolarPaces Conference*, (November 2011), 2011.

[30] A. S. Khalid. *Development and implementation of rotorcraft preliminary design methodology using multidisciplinary design optimization*. PhD thesis, Georgia Institute of Technology, 2006.

[31] D. P. Schrage. Teaching graduate rotorcraft design based on twenty years of experience. *age*, 10: 1, 2005.

[32] J. H. Davis. *Design methodology for developing concept independent rotorcraft analysis and design software*. PhD thesis, Georgia Institute of Technology, 2007.

[33] Ø. Magnussen, G. Hovland, and M. Ottestad. Multicopter uav design optimization. In *2014 IEEE/ASME 10th International Conference on Mechatronic and Embedded Systems and Applications (MESA)*, pages 1–6. IEEE, 2014.

[34] Ø. Magnussen, M. Ottestad, and G. Hovland. Multicopter design optimization and validation. 2015.

[35] X. Dai, Q. Quan, and K.-Y. Cai. Design automation and optimization methodology for electric multicopter uavs. *arXiv preprint arXiv:1908.06301*, 2019.

[36] B. Meindl and M. Templ. Analysis of commercial and free and open source solvers for linear optimization problems. *Eurostat and Statistics Netherlands within the project ESSnet on common tools and harmonised methodology for SDC in the ESS*, 20, 2012.

[37] O. Gur and A. Rosen. Optimizing electric propulsion systems for uavs. In *12th AIAA/ISSMO Multidisciplinary Analysis and Optimization Conference*, page 5916, 2008.

[38] J. M. Winslow, V. Hrishikeshavan, and I. Chopra. Design methodology for small scale unmanned quadrotors. In *55th AIAA Aerospace Sciences Meeting*, page 0014, 2017.

[39] M. Gatti and F. Giulietti. Preliminary design analysis methodology for electric multirotor. *IFAC Proceedings Volumes*, 46(30):58–63, 2013.

[40] S. Bouabdallah and R. Siegwart. Design and control of a miniature quadrotor. In *Advances in unmanned aerial vehicles*, pages 171–210. Springer, 2007.

[41] T. Ng and G. Leng. Design of small-scale quadrotor unmanned air vehicles using genetic algorithms. *Proceedings of the Institution of Mechanical Engineers, Part G: Journal of Aerospace Engineering*, 221(5):893–905, 2007.

[42] D. Bershadsky, S. Haviland, and E. N. Johnson. Electric multirotor uav propulsion system sizing for performance prediction and design optimization. In *57th AIAA/ASCE/AHS/ASC Structures, Structural Dynamics, and Materials Conference*, page 0581, 2016.

[43] C. Ampatis and E. Papadopoulos. Parametric design and optimization of multi-rotor aerial vehicles. In *Applications of Mathematics and Informatics in Science and Engineering*, pages 1–25. Springer, 2014.

[44] ecalc. `https://www.ecalc.ch/xcoptercalc.php`. Accessed: 2019-09-30.

[45] J. A. Benito, G. Glez-de Rivera, J. Garrido, and R. Ponticelli. Design considerations of a small uav platform carrying medium payloads. In *Design of Circuits and Integrated Systems*, pages 1–6. IEEE, 2014.

[46] N. M. Kumar, K. Sudhakar, M. Samykano, and V. Jayaseelan. On the technologies empowering drones for intelligent monitoring of solar photovoltaic power plants. In *Procedia Computer Science*, volume 133, pages 585–593. Elsevier, jan 2018. doi: 10.1016/j.procs.2018.07.087. URL `https://www.sciencedirect.com/science/article/pii/S1877050918310366`.

[47] Aerones. `https://www.aerones.com/eng/wind_turbine_maintenance_drone/`. Accessed in June 2019.

[48] pro-drone. `https://www.pro-drone.eu/`. Accessed: 2019-09-30.

[49] F. Technology. Drone inspection of power lines and civil infrastructure. `https://forcetechnology.com/en/services/drone-inspection-of-power-lines-and-civil-infrastructure`. Accessed in June 2019.

[50] J.-M. Tarascon and M. Armand. Issues and challenges facing rechargeable lithium batteries. In *Materials for Sustainable Energy: A Collection of Peer-Reviewed Research and Review Articles from Nature Publishing Group*, pages 171–179. World Scientific, 2011.

[51] D. Bershadsky, S. Haviland, and E. N. Johnson. Electric multirotor uav propulsion system sizing for performance prediction and design optimization. In *57th AIAA/ASCE/AHS/ASC Structures, Structural Dynamics, and Materials Conference*, page 0581, 2016.

[52] V. Bertram and V. Bertram. Chapter 2 – Propellers. In *Practical Ship Hydrodynamics*, pages 41–72. Butterworth-Heinemann, jan 2012. ISBN 9780080971506. doi: 10.1016/B978-0-08-097150-6.10002-8. URL https://www.sciencedirect.com/science/article/pii/B9780080971506100028.

[53] W. Johnson. Helicopter theory, 1994. *Dover Publications*, 1994.

[54] K. Palanduz. Experimental Analysis of a Variable Pitch Multi-rotor Propeller. (October), 2017.

[55] J. Seddon and S. Newman. Basic helicopter aerodynamics, american institute of aeronautics and astronautics. *Inc., Reston, VA*, 2001.

[56] Filipe Szolnoky Cunha-Instituto Superioir Tecnico. *Helicopters-Momentum Theory*. URL https://fenix.tecnico.ulisboa.pt/downloadFile/282093452028191/3-MomentumTheoryinhover.pdf.

[57] A. Raptopoulos, D. Damm, M. Ling, and I. Baruchin. Transportation using network of unmanned aerial vehicles, July 5 2016. US Patent 9,384,668.

[58] T-motor. http://uav-en.tmotor.com/. Accessed: 2019-09-30.

[59] O. Magnussen, G. Hovland, and M. Ottestad. Multicopter UAV design optimization. In *2014 IEEE/ASME 10th International Conference on Mechatronic and Embedded Systems and Applications (MESA)*, pages 1–6. IEEE, sep 2014. ISBN 978-1-4799-2280-2. doi: 10.1109/MESA.2014.6935598. URL http://ieeexplore.ieee.org/document/6935598/.

[60] Z. Liu, R. Sengupta, and A. Kurzhanskiy. A power consumption model for multi-rotor small unmanned aircraft systems. In *2017 International Conference on Unmanned Aircraft Systems (ICUAS)*, pages 310–315. IEEE, 2017.

[61] G. Ononiwu, A. Okoye, J. Onojo, and N. Onuekwusi. Design and implementation of a real time wireless quadcopter for rescue operations. *American Journal of Engineering Research (AJER)*, 5 (9):130–138, 2016.

[62] H. Zhang, J. Baeyens, J. Degrève, and G. Cacères. Concentrated solar power plants: Review and design methodology. *Renewable and sustainable energy reviews*, 22:466–481, 2013.

[63] S. Muhamad, H. M. Nasir, S. Kari, and M. S. M. Ali. Hovering recovery strategies for single rotor inoperative quadcopter. *Int. J. of Applied Eng. Res*, 12:24, 2017.

[64] P. Ventura Diaz and S. Yoon. High-fidelity computational aerodynamics of multi-rotor unmanned aerial vehicles. In *2018 AIAA Aerospace Sciences Meeting*, page 1266, 2018.